UCLouvain

École polytechnique de Louvain

Analysis and Design of 1D Metasurface Antennas

Author: **Sophie Van Wynendaele**
Supervisors: **Christophe Craeye, Jean-Pierre Raskin**
Readers: **Modeste Bodehou, Dimitri Lederer**
Academic year 2020–2021
Master [120] in Electrical Engineering

Preface and Acknowledgements

The present Master Thesis contributes to obtaining the Master in Electrical Engineering at UCLouvain. The work addresses the issue related to the analysis and design of metasurface antennas. This emerging technology is inherently very low profile, which makes it very attractive in the electromagnetic community. The technology is not yet fully mature but offers unique properties that many researchers are exploring. The algorithms proposed in this thesis have been developed in Matlab platform, with some C/C++ extensions.

This last academic year allowed me to develop my knowledge in the field of antennas, and more particularly, that of metasurfaces. I also interacted with many people who have contributed to the achievement of my thesis.

First of all, I would like to thank Professor Christophe Craeye and Modeste Bodehou, who accompanied me throughout the realization of this thesis. Mr. Craeye, thank you for your unfailing availability, analysis, and feedback on my work, which allowed me to improve all along the year. I also address my special thanks to Modeste, who allowed me to achieve and present quality work. Thank you for your great investment and for all that you have transmitted to me during these last months.

I would also like to thank other researchers from the EPL antenna group, Husnain Ali Kayani and Jean Cavillot, who helped me get started with the laboratory code and validated some of my results.

Near-field measurements was one of the initial objectives of the thesis. Due to time constraints it was decided to not cover this topic in the thesis. Nevertheless, I really thank Professor Jean-Pierre Raskin, in charge of this part, who guided me when I needed it. I would also like to thank Sébastien Toussaint, Mojtaba Razavian and Maxime Drouguet, who contributed to implementing the near field test bench and preparing the first measurements.

Finally, a big thank you to my parents and my sister. You have helped and encouraged me daily, and this since the beginning of my studies. Your help, even indirect, in the realization of this thesis was really precious.

Abstract

Metasurfaces (MTS) are artificially engineered 2D structures that exhibit, in a given frequency band, macroscopic (at the wavelength scale) properties that go beyond those of usual surfaces. Metasurface sheets are commonly implemented as a dense array of subwavelength scatterers, possibly printed on a grounded slab. They can be designed to arbitrarily transform an incident wave in reflection or in transmission. In this thesis, metasurfaces are designed to manipulate the dispersion characteristics of excited surface waves (SW) to progressively transform those surface waves into leaky waves (radiation). A 1D metasurface antenna is considered, which is assumed to be fed by a plane wave SW launcher. The MTS is modelled as a modulated impedance sheet laying on a grounded slab. The design procedure proposed in this thesis is decomposed into three stages.

First, the analysis of the current distribution along MTS antennas is performed through simulations based on the solution of integral equations for the electric field (EFIE). The resulting linear system of equations is solved into a set of orthogonal basis functions using the Method of Moments (MoM).

Then, the design of MTS antennas is realized through the modification of the surface impedance to achieve the desired radiation characteristics. Based on the a priori knowledge of the currents from the desired radiation pattern, the surface impedance, decomposed into pre-determined basis functions, is computed.

The last step of the design procedure is the implementation of the computed surface impedance with metal patches to obtain the physical structure of the antenna. The implemented design procedure is applied to different patterns of increasing complexity: a simple pencil beam, multibeams and a flat-top beam.

Keywords : metasurface, antenna, 1D, design, EFIE, MoM, patches, leaky-wave

Contents

List of Figures

List of Tables

Acronyms and Abbreviations

EFIE	Electric-field integral equation.
FD	Finite-Difference method.
FEM	Finite-Element method.
IBCs	Impedance Boundary Conditions.
LW	Leaky-Wave.
MoM	Method of Moments.
MTS	Metasurface.
RP	Radiation Pattern.
SW	Surface Wave.
TM	Transverse magnetic.

Introduction

The first antennas appeared at the end of the 19th century following the discoveries of induction phenomena by Michael Faraday (1831) and especially the theoretical developments resulting from Maxwell's equations (1873). If the first antennas were made exclusively of wires, they quickly developed into more complex and efficient structures to expand the development of wireless information transmission. Progress in this area has been rapid because it affects radio transmissions where the number of applications is considerable. Communication systems continue to evolve over the years in response to ever-increasing performance requirements. Very mature technologies such as antenna arrays make it possible to meet most expectations, such as a high gain, beam shaping or beam scanning. Also, they allow the diversity that is required for new communications systems based on Multiple-Input Multiple-Output (MIMO) techniques. Today, in the space field and applications linked to 5G, the trend is towards the miniaturization and compactness of antennas while maintaining a high directivity and arbitrary aperture design.

In this attractive market, metasurface (MTS) antennas appear as an innovative technology, opening new opportunities to design low-cost antennas. Being lightweight and not very complex to manufacture, these antennas receive a growing interest due to their electromagnetic properties unattainable with conventional devices and materials. These characteristics are not dictated by the atomic and molecular constitution of the materials but by their macroscopic properties obtained from an engineering process. Indeed, negative permittivity and permeability can be obtained by arranging, at the wavelength scale, small shaped elements on the surface of a substrate. Therefore, a MTS antenna is characterized by a set of metal subwavelength patches printed on its surface. In Fig. 1 is given a prototype of a MTS antenna.

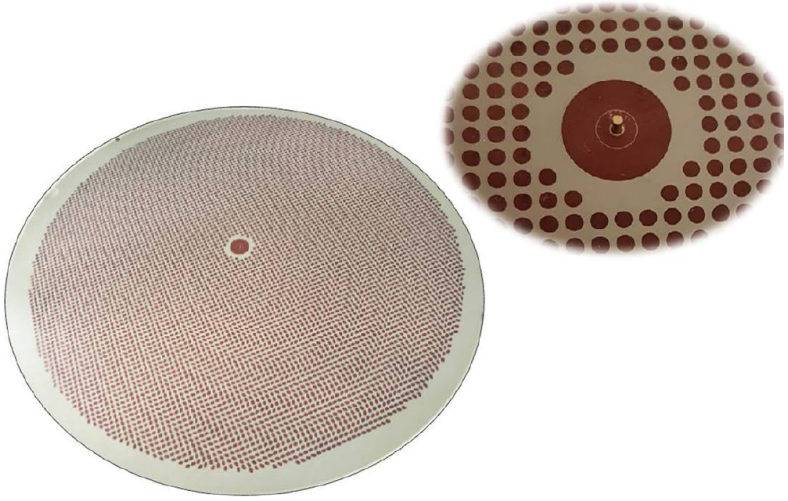

Figure 1: Example of a metasurface antenna with details of the feeder and patches structure [1].

The manipulation of electromagnetic waves comes from the progressive interaction between these patches and a surface wave generated by the feed. The phenomenon is represented in Fig. 2. The wave coming from the feed is scattered by the patches and this results in the creation of leaky-waves. Orientation of the leaky-waves allows the antenna to radiate in a specific direction (see Fig. 3). Designing a MTS antenna boils down to modifying the layout and orientation of the patches to achieve the desired radiation characteristics. Changes to this patch layer can be interpreted as a surface impedance modulation.

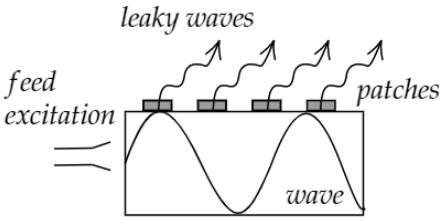

Figure 2: Leaky-wave antenna.

This thesis focuses more particularly on the analysis and design of 1D metasurface antennas. The 1D case is a simplified version of what is mainly found in the literature. However, it still allows approaching a large part of the concepts covered by this field of research. Also, the new design technique for MTS antenas, as developed at UCLouvain, has never been applied to 1D metasurfaces, which required very specific adaptations. This thesis discusses the analysis and design procedure of 1D metasurface antennas throughout four chapters.

A review of the literature in Chapter 1 examines the current situation of MTS antennas technology. General concepts are also presented regarding antennas and numerical simulation, allowing the introduction of essential bases for a good understanding of the content of the thesis.

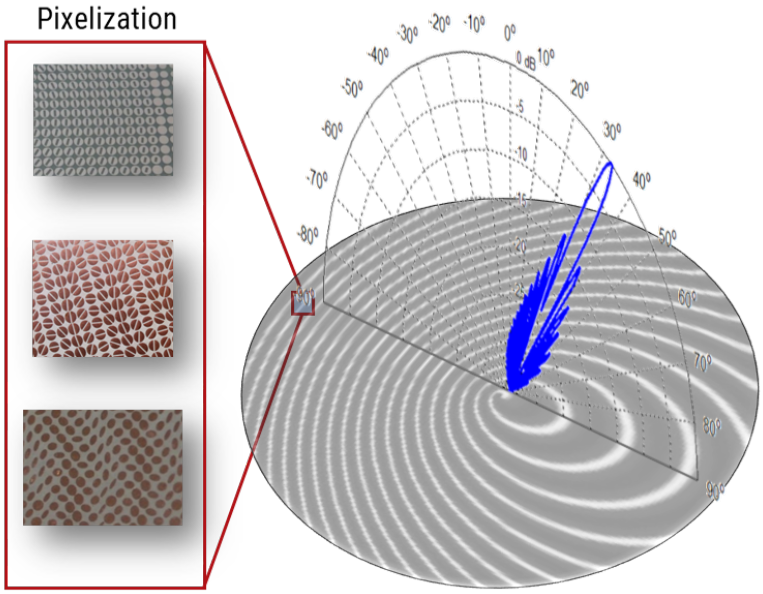

Figure 3: Metasurface antenna with its radiated beam and some examples of patches configuration.

The following chapters detail the three essential steps to complete a quasi-direct method for designing 1D MTS antennas. By quasi-direct one means that there will be essentially no optimization, despite the fact that the antenna can be characterized by order of 100 parameters (thousands in the 2D case).

First, the analysis of the current distribution along the antennas is performed through the solution of Maxwell's equations in integral form. Those equations contain the unknown current distribution, which is described as a linear combination of orthogonal functions. In the end, it consists of solving a system of linear equations.

The second step of the design procedure is the most expensive in terms of computational complexity. It consists of solving the opposite problem to the one introduced during the analysis. One tries to determine the antenna's surface impedance, which allows, following coupling with the surface wave, to radiate the desired pattern. Several designs are presented for the following radiation characteristics: a pencil beam, multibeams, and a flat top beam.

Finally, the last step of the design procedure is to implement the computed surface impedance using metal patches. It results in a physical structure of the antenna that one can simulate to compare its radiation pattern to the desired one. All the simulations are carried out using the MATLAB® software and particular C and C++ extensions for the most intensive operations.

Chapter 1

Theoretical context

1.1 Review of the literature

1.1.1 Metasurface

Metamaterials are materials which, as the literal Greek translation of this word indicates, offer properties "beyond" the "matter". Behind this promising translation one finds structured materials, resulting from an engineering process. They exhibit properties that are not found naturally, such as negative permittivity and/or permeability. Metamaterials are characterized, on a subwavelength scale, by periodic structures composed of small scatterers (see Fig. 1.1(a)). Non-typical properties are observed when these scatterers are resonantly coupled to the electric and magnetic fields of the incident electromagnetic waves [2]. It is, therefore, not the intrinsic characteristics of the materials that interets us. In fact, this is the way the materials are spatially distributed that open the way to these new properties. Metamaterials are very promising despite challenges due to high losses and frequency dispersion due to their resonant responses under excitation [3].

Over the past twenty years, metamaterials have moved from being simply a theoretical concept to a field with developed and marketed applications. By extending these metamaterials to their 2D version, we opened the way to the study of textured surfaces at the subwavelength scale called *metasurfaces* (MTS)[1]. By playing on the composition, shape and orientation of scatterers arranged periodically, it is possible to manipulate electromagnetic waves (see Fig. 1.1(b)). Those manipulations are done at the subwabelength scale, allowing aperture fields to be controlled in phase, amplitude and polarization. Metasurfaces make this possible by supporting leaky-waves that directly radiate according to specified

[1]This introductory chapter discusses metasurface antennas in general and is therefore not focused on the 1D case specific to the thesis.

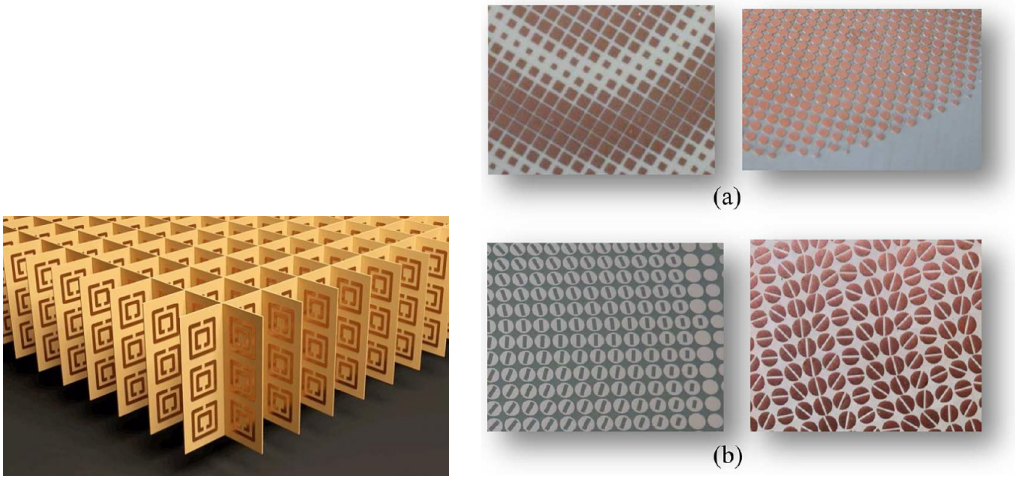

(a) Example of metamaterial [5]

(b) Examples of IBC implementations using metal patches [6]

Figure 1.1: Examples of metamarial and metasurfaces.

radiation patterns [4]. Leaky-wave antennas is the subject of the following section and, more generally, that of the thesis.

1.1.2 Modulated metasurface antennas

Modulated metasurface antennas correspond to a class of the leaky-wave (LW) antennas. They are characterized by small metallic or dielectric patches printed on a grounded slab. When the patches interacts with a travelling TM surface-wave (SW) coming from the feed, the antenna radiates (see Fig. 2). The progressive interaction induced leakage of power and allows the control of the amplitude, phase and polarization of radiated fields. The size, position and orientation of the patches are parameters to play with in order to achieve the desired radiation performance. Fig. 1.1(b) shows different patches arrangements of increasing complexity. Polarization of the radiated fields can be controlled using patches containing features like slots (image (b) of Fig. 1.1(b)). In the context of this thesis, we will consider simple square patches like those present in image (a).

The layer of metallic patches allows characterizing the surface of the antenna in terms of impedance. Once the substrate is covered with the patches, the surface of the antenna is constrained to modulated impedance boundary conditions (IBCs) [6]. IBC can be modulated by changing the arrangement and physical structure of the patches. Modifying the MTS patches' structure leads to beam tilting, beam

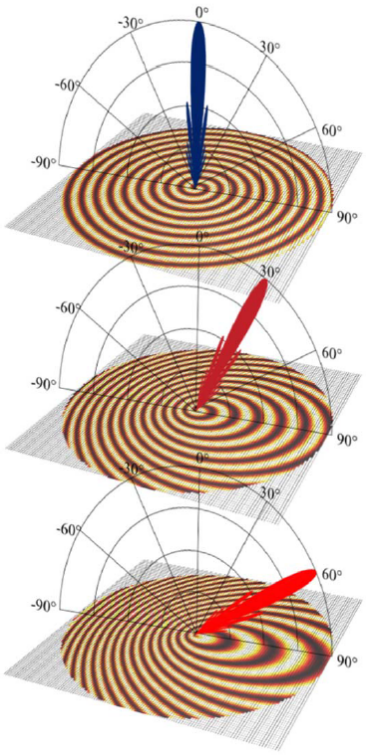

Figure 1.2: Beam sweeping by changing the IBC of the MTS [4].

shaping, and polarisation control. An example is shown in Fig. 1.2 where changing the IBC of the MTS allows modification of the pointing of the main beam.

To understand basic principle behind leaky-wave antennas and, in particular, modulated MTS antennas one have to introduce the notion of spectral domain.The coordinates of the spectral domain (k_x, k_y, k_z) allow the decomposition of the fields into a continuum of plane waves defined by

$$E_0 e^{-j(k_x x + k_y y + k_z z)} \tag{1.1}$$

The amplitude E_0 and the spectral coordinates are orthogonal to each other. k_z is related to the wavenumbers k_x and k_y through the following relation

$$k_x^2 + k_y^2 + k_z^2 = k^2 = \frac{2\pi}{\lambda} \tag{1.2}$$

with the associated wavelength λ. Decomposing the fields into complex exponentials amounts to calculating a Fourier Transform to obtain the antenna's radiation pattern. One will develop this notion in Section 1.2.2.

The spectral domain contains two zones (see Fig. 1.3) :

- the visible region: $\sqrt{k_x^2 + k_y^2} \in [-k_0; k_0]$
- the invisible region: $\sqrt{k_x^2 + k_y^2} > k_0$

with k_0 the free-space wavenumber.

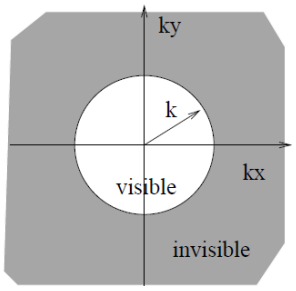

Figure 1.3: Visible and invisible zones of the spectral domain [7].

Principle of leaky-wave antenna is represented in Fig. 1.4. We consider first the upper configuration where we have a constant capacitive surface impedance supporting the propagation of TM SWs. In this case, the wavenumber k_{sw} of the surface wave is outside the visible region, and therefore the SW does not radiate. To radiate, harmonics (Floquet modes) of the fundamental SW must fall in the visible region. This phenomenon appears when adding a modulation at the wavelength scale to the previous average constant impedance (see second configuration illustrated in Fig. 1.4). We observe that one harmonic is present in the visible region, leading to radiation.
In practice, it is the radiation harmonic $k_{n=-1}$ which radiates. The design of a metasurface antenna (determining its surface impedance) therefore amounts to matching the desired radiating aperture field with the -1 harmonic.

1.1.3 Applications and challenges

This section will highlight the opportunities offered by MTS, which are favourable to their use in many applications and the issues that still need to be addressed to pave the way for their development at a large scale.

First, MTS results in a light and compact structure, which makes them good candidates for the space field for which this type of antenna was initially designed [6]. In addition to these exciting characteristics, we have their cost, which is notably attractive due to light manufacturing process. Generally, it requires, in addition to standard PCB techniques, standard lithography or the use of 3D printing equipment.

Furthermore, by having the capacity to produce an arbitrary aperture field, MTSs can become a low-cost alternative to phased arrays. Phased array is a mature and efficient technology today, which however comes with large feed network losses and high cost.

The use of MTS could be extended to many wireless communication applications such as 5G, for which the compactness of the antennas is essential. However, this kind of applications requires a wide bandwidth to achieve a higher data transfer

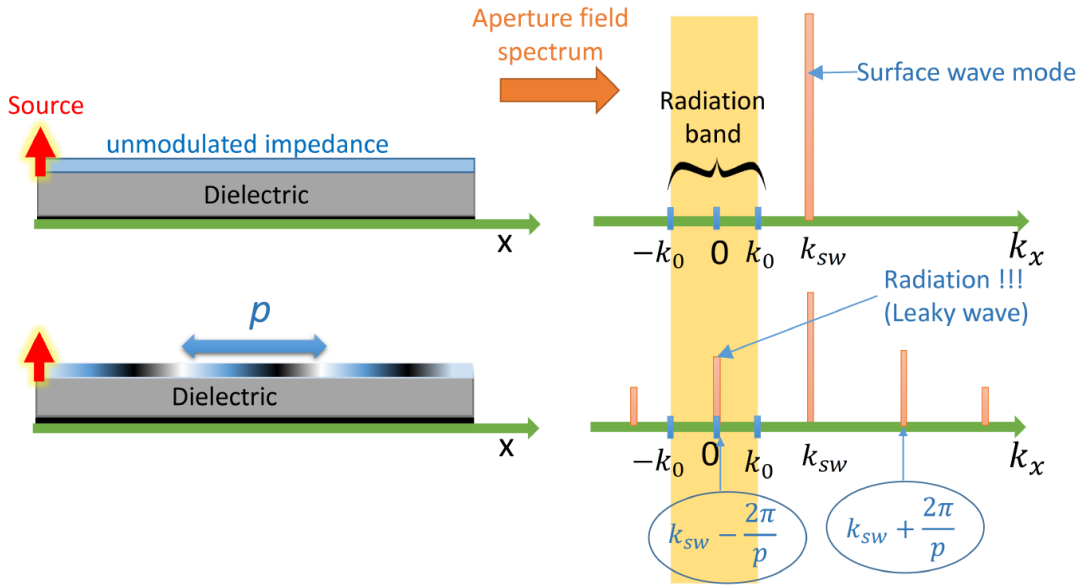

Figure 1.4: Spectral representation of the aperture fields produced by an antenna with constant surface impedance and by modulated MTS antenna [8].

rate. This is where we meet the first challenges because antenna pattern stability versus frequency is needed to fulfil this requirement. With MTSs, the stability with frequency is mainly limited by the mismatch between the SW wavelength and the periodicity of the IBCs. Instabilities occur when the operational frequency moves away from the frequency at which the antenna has been designed [4]. Nevertheless, in reference [1] antennas with a relative operational bandwidth up to 30% have been reported.

While the solutions linked to the challenge described above are rapidly progressing, it is not yet the case for those allowing the adaptivity of MTSs for fast beam hopping, another essential feature for 5G applications. Research on electronically reconfigurable MTS antennas is growing to allow the reconfiguration of the beam quickly through mechanically [9] or electronically [10] tunable textured surfaces. The adaptation of such antennas to curved surfaces for aerodynamic applications is one more challenge on the list [11].

Although very promising, the wide deployment of MTS antenna is held back by challenges that still must be overcome.

1.2 Antenna related concepts

This section aims to introduce some notations and essential theoretical bases of certain constitutive elements of the developments and strategies encountered throughout the thesis.

1.2.1 Green's functions in layered substrates

The following mathematical derivations come from reference [12]. The main results are described but the reference contains further information and rigorous proofs, including the theory of transmission lines applied to waves in multi-layered media.

In this thesis, we will need the Green's function to calculate the field radiated by a given current distribution. Knowing that the Green's function determines the field radiated by a unit point-current for a specific polarization, it is possible to determine the field radiating from a known current distribution

- In the *spatial* domain, using a convolution:

$$\mathbf{E}(\mathbf{r}) = \mathbf{G}(\mathbf{r}, \mathbf{r}') * \mathbf{J}(\mathbf{r}') \tag{1.3}$$

- In the *spectral* domain, using a product:

$$\widetilde{\mathbf{E}}\left(k_x, k_y\right) = \widetilde{\mathbf{G}}\left(k_x, k_y\right) \widetilde{\mathbf{J}}\left(k_x, k_y\right) \tag{1.4}$$

with $\mathbf{r}$ the point at which the field is evaluated, $\mathbf{r}'$ the point at which the source is located, k_x and k_y the spectral coordinates. $\mathbf{J}$ ($\widetilde{\mathbf{J}}$) and $\mathbf{G}$ ($\widetilde{\mathbf{G}}$) are respectively the source current and the Green's function in the spatial (spectral) domain.

In layered substrates, the Green's function consists of two potentials: $\widetilde{G_A}$ and $\widetilde{G_V}$. Their derivation is present in the reference cited above, but we will not recall them here. In layered substrates and spectral domain, Green's functions become

$$\widetilde{\mathbf{G}}\left(k_x, k_y\right) = \widetilde{G}_A \mathbf{I} + \widetilde{G}_V \begin{bmatrix} k_x^2 & k_x k_y \\ k_x k_y & k_y^2 \end{bmatrix} \tag{1.5}$$

with $\mathbf{I}$ the identity matrix. These potentials are scalar and depend only on the norm of k_x and k_y. This property makes their tabulation easy, unlike a tensorial Green function which takes into account the vectorial character of currents and fields.

1.2.2 Radiation pattern

The radiation pattern (RP) is a representation of the distribution of radiated field into space as a function of direction. In the spectral domain, it gives

$$\mathbf{F}\left(k_x, k_y\right) = \frac{-j}{\lambda}\left[\hat{u} \times \hat{n} \times \widetilde{\mathbf{E}}\left(k_x, k_y\right)\right] \tag{1.6}$$

with $\hat{n}$ the normal to the surface, $\hat{u}$ the unitary vector for the direction of observation and $\widetilde{\mathbf{E}}$ the 2D Fourier transform of the aperture electric field. It results in a function depending on the direction of observation, given by the normalization of the wavevector (k_x, k_y, k_z).

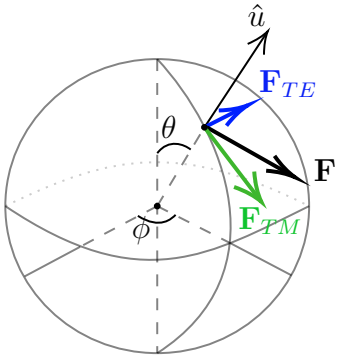

Figure 1.5: Pattern representation in the TE-TM basis.

For a more physical representation, we will project the radiation pattern in a TE-TM base (Fig. 1.5).

$$\begin{bmatrix} F_{TE}\left(k_x, k_y\right) \\ F_{TM}\left(k_x, k_y\right) \end{bmatrix} = \begin{bmatrix} -\sin(\phi) & \cos(\phi) & 0 \\ \cos(\phi)\cos(\theta) & \sin(\phi)\cos(\theta) & -\sin(\theta) \end{bmatrix} \begin{bmatrix} F_x\left(k_x, k_y\right) \\ F_y\left(k_x, k_y\right) \\ F_z\left(k_x, k_y\right) \end{bmatrix} \tag{1.7}$$

1.2.3 Directivity

Directivity $D(\theta, \phi)$ is obtained as the ratio between the power per unit angle in the direction of interest $U(\theta, \phi)$ and the average power per unit angle P_{tot} [13].

$$D(\theta, \phi) = 4\pi \frac{U(\theta, \phi)}{P_{\text{tot}}} \tag{1.8}$$

$$P_{\text{tot}} = \int_{\phi}\int_{\theta} U(\theta, \phi)\sin(\theta) d\theta d\phi \tag{1.9}$$

with $U(\theta, \phi) = |F_{TE}(\theta, \phi)|^2 + |F_{TM}(\theta, \phi)|^2$. This normalisation can also be applied individually to F_{TE} and F_{TM}.
Directivity is used to compare results of numerical simulations in Chapters 3 and 4.

1.2.4 Radiated power

The complex power P_c radiated by an aperture is given by [7]

$$P_c = \frac{1}{k_0 120\pi} \iint_{-\infty}^{\infty} |\widetilde{\mathbf{E}}\left(k_x, k_y\right)|^2 k_z^{\star}\, dk_x dk_y \tag{1.10}$$

with $k_z = \sqrt{k_0^2 - k_x^2 - k_y^2}$ and $\widetilde{\mathbf{E}}$ the 2D Fourier transform of the aperture electric field.

By integrating over the whole (k_x, k_y) domain, the radiated power is complex. However, the visible domain contributes to active power and the invisible domain to reactive power. Only the real part will be of interest for us in the following because it corresponds to the power truly radiated by the metasurface antenna.

1.3 Method of Moments

1.3.1 Electromagnetic problem solving

To compute electromagnetic fields for a given excitation in a given materials configuration, there exist a large number of numerical methods. The main basis of those methods is Maxwell's equations that we can formulate in integral or differential forms. Depending on the application and the unknown we want to obtain, different methods can be considered [14]. In particular, we can highlight two distinct groups of techniques. The first aims at the direct solution for the magnetic or electric field while the second group aims at determining currents, either physical or equivalent ones. From those currents, fields can be delineated in a second phase.

In the first group, we find the Finite-Element method (FEM) and the Finite-Difference method (FD), which use Maxwell's equations (or their derivatives) in their differential form. With these methods, non-linearities can be treated, as well as complicated shapes of radiating structures. The system of equations to be solved is easy to construct, and we end up with a sparse matrix. The drawbacks of these methods are the large number of unknowns and the high quality required for the mesh [15].

The second group aims at solving integral equations whose unknowns are the sources of analyzed fields (or potentials from which fields can be derived). The main subject of this section, the Method of Moments (MoM), is part of this second group of numerical solution techniques.

1.3.2 Formulation and intuition of the Method of Moments

With MoM, we want to resolve an integral equation to compute the current distribution on an antenna. This kind of equation belongs to the general class of linear operator equations. We can write it with a general expression [16]

$$L(f) = g \tag{1.11}$$

where L is an integral operator. This expression links a known function g that models the excitation of the antenna to an unknown quantity f we want to determine, i.e., the currents.

The interest of the method lies in the approximation of the unknown quantity f as a finite sum of known functions of lower complexity f_n (named *basis* or *expansion* functions).

$$f \approx \sum_{n=1}^{N} \alpha_n f_n \tag{1.12}$$

The scalar coefficients α_n become the unknowns to determine. The functions f_n are chosen such that N is small and the function f is approximated as well as possible. We substitute (1.11) into (1.12), and by linearity of the operator L we have

$$\sum_{n=1}^{N} \alpha_n L\left(f_n\right) \approx g \tag{1.13}$$

As (1.13) is an approximation, it is necessary to introduce a measure of accuracy to determine the unknowns α_n while equalising the two members of the equation as well as possible. This measure implies an inner product of the equation (1.13) that is multiplied by chosen and known *testing* functions (also named *weighting* functions) w_m. The inner product, generally an integral over a spatial region giving scalars, offers the linearity property, thanks to which we obtain

$$\sum_{n=1}^{N} \alpha_n < w_m, L\left(f_n\right) > = < w_m, g >, \quad m \in [1; N] \tag{1.14}$$

As equation (1.14) indicates, the testing is carried out for a set of N functions w_n. We can therefore rewrite the problem in a matrix form

$$\begin{aligned} \mathbf{A}\mathbf{x} &= \mathbf{b} \\ \text{with} \quad \mathbf{A} &= < w_m, L\left(f_n\right) > \\ \mathbf{x} &= \alpha_n \\ \mathbf{b} &= < w_m, g > \end{aligned} \tag{1.15}$$

Contrary to the FEM mentioned in section 1.3.1, the MoM results in a dense system of equations that one can solve using the LU decomposition or Gaussian elimination.

From the concept of residual defined below and derived from (1.13), we can use the projection theory to have an intuition about what's going on behind the MoM resolution.

$$r = g - \sum_{n=1}^{N} \alpha_n L\left(f_n\right) \tag{1.16}$$

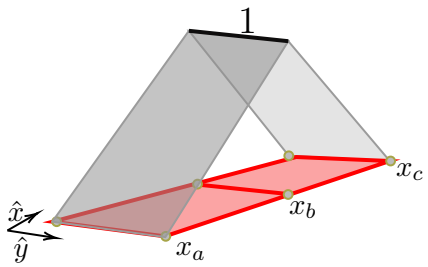

Figure 1.6: Rooftop basis function.

In projection theory, the MoM amounts to defining the α_n such that the residual r is orthogonal to each w_m. In other words, r must be equal to zero in the testing subspace. In fact, (1.14) is verified when $< w_m, r >= 0$.

1.3.3 Choice of basis and testing functions

The choice of basis and testing functions is essential because it influences the approximation of f and the quality of its measurement. A good choice also minimises the number of functions used and, therefore, the complexity of the method. These functions can be of two types, depending on their domains of definition:

- *Subdomain functions :* The domain of interest defining the unknown function f (e.g., the surface of the antenna) is divided into several subdomains. Therefore, a basis (or testing) function is defined only on this subdomain and vanishes otherwise. In this category, we find the rooftop function (see Fig. 1.6). This basis function will be detailed in the following section because rooftops are used within the framework of the thesis.

- *Entire-domain functions :* Each basis (or testing) function is defined on the whole domain of the unknown function f. They can be of the polynomial or even trigonometric type.

1.3.4 MoM in the framework of the thesis

The Method of Moments is used in the framework of this thesis to resolve the electric field integral equation (EFIE). This equation links, through integrals, the incident fields to the currents. We can make the link between the EFIE and the MoM system (1.14) by identifying the unknown α_n to be the currents i_n and g the

incident fields, known a priori.

$$\sum_{n=1}^{N} i_n < w_m, L(f_n) > =< w_m, g >, \quad m \in [1; N] \tag{1.17}$$

We can reformulate the last expression in a system of linear equations

$$\mathbf{Zi} = \mathbf{v} \tag{1.18}$$

where the vector $\mathbf{v}$ is known and contains the tested incident fields. To solve numerically (1.18), we must have the mesh of the antenna, its operating frequency as well as all the information concerning the substrate.

Resolution is done through the use of a MoM code developed by the EPL Antenna Laboratory via the MATLAB® software as well as C/C++ code for the most intensive operations [17]. The code uses rooftops as basis functions to mesh the structure of the antenna. The same rooftops are used as testing functions. We called that Galerkin testing and have therefore $f_n = w_m, \forall n$. More explanations on the practical definition of these basis functions in the code are given in Appendix A. The MoM code computes the impedance matrix $\mathbf{Z}$ then resolve for the currents $\mathbf{i}$. One have finally access to the current distribution, and it is possible to compute the radiation pattern of the antenna.

1.4 Summary of the general design procedure

This section provides an overview of the design procedure of 1D MTS antennas developed in this thesis. The latter is divided into three phases, represented in Fig. 1.7. The objectives pursued by the analysis, synthesis and implementation of 1D MTS antennas are briefly discussed in the lines that follow. Subsequent chapters provide in-depth explanations and results about what has been achieved for those three stages.

Analysis of 1D modulated metasurface antennas

Numerical analysis of MTS antenna aims at obtaining the surface currents and resulting radiation pattern. It is very complicated and heavy in terms of complexity of simulations. In fact, a simulation of the antenna must consider all the patches present on its surface, designed at a subwavelength scale. The meshes used to perform MoM simulations with the lab code are very dense because they are composed of subdomain basis functions (rooftops). To alleviate the calculations, the use of macro-basis functions will be introduced. Those functions, defined over the entire domain, will make it possible to analyze the antenna without mesh and

with a reduced number of functions.

Synthesis of 1D modulated metasurface antennas

The synthesis stage aims to determine the surface impedance distribution that radiates, in contact with the SW, a desired radiation pattern. Surface impedance is purely imaginary, and we know its general expression, characterized by a modulation $P(x)$ applied to an average value jX_0.

$$Z(x) = jX_0 + P(x) \tag{1.19}$$

To determine the unknown $Z(x)$, we will expand it into a set of basis functions according to the same principle as the Fourier series decomposition. The coefficients obtained in this new base will become the unknowns of the problem.

Implementation of 1D modulated metasurface antennas

Implementation is the last step in the design process. It consists of implementing with patches the impedance determined in the previous step. Considering the case of 1D and isotropic antennas, the only parameter to be determined will be the size of the patches. They will discretize the aperture of the antenna and will be square, of size not exceeding $\lambda/7$.

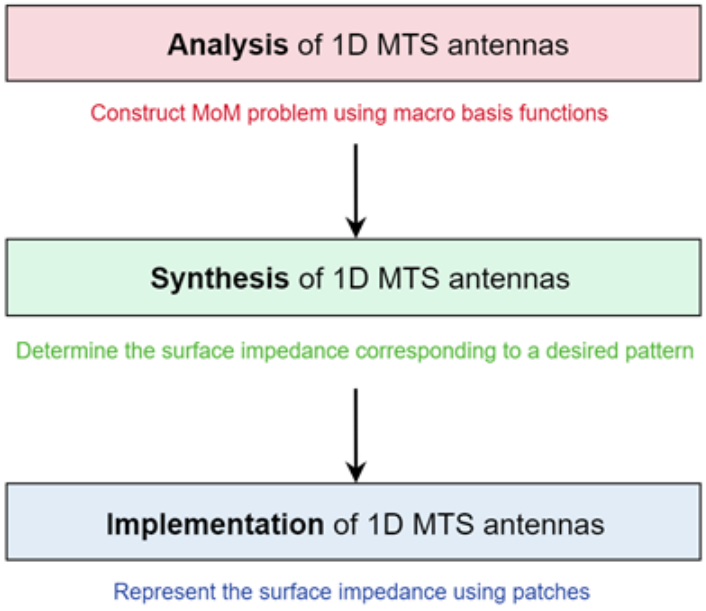

Figure 1.7: Overview of the design procedure of 1D MTS antennas developed in this thesis.

Chapter 2

Numerical analysis of 1D modulated metasurface antennas

This chapter details the first stage of the design procedure: the analysis of 1D modulated metasurface antennas. The simulation of MTS antennas with the MoM method can be realized using two types of basis and testing functions; subdomain and entire-domain functions. These were introduced in Section 1.3.3.

The first case, subdomain functions, is the one implemented in the MoM code of the antenna laboratory. The code uses rooftop functions to mesh the structure. The number of rooftops become quickly important when it comes to mesh numerous patches (around 3700 functions in this thesis). This very dense mesh causes relatively long simulation times. Simulations of this type are carried out at the beginning of this chapter based on an antenna design taken from the literature. This design comes from the paper "A printed leaky-wave antenna based on a sinusoidally-modulated reactance surface" by Amit Patel and Anthony Grbic [18]. This paper describes a simple procedure for designing a 1D sinusoidally modulated reactance surface to generate a desired directional radiation at a certain angle and for a particular frequency. The authors realized an antenna radiating at 30 degrees from broadside at 10 GHz. A surface impedance is therefore proposed, implemented, and then validated experimentally.

In the following section, results from MoM simulations of this proposed surface impedance are compared with those from the paper. Also, the exploration of the impact of some specific design parameters on the antenna is done.

After the rooftops, the entire-domain basis functions will be used in this chapter. This second type of basis functions allows to resolve integral equations with the MoM in a set of basis functions defined over the entire antenna domain. Using these functions decreases the complexity of the algorithms because their

number is significantly reduced compared to the first case described above. Typically, their number will never exceed 250 in simulations generated for this thesis.

The use of these continuous functions is not supported by the code of the antenna laboratory. This thesis therefore describes the formulation and the construction of a MoM system of equations where those functions can be used to simulate metasurface antennas. The new MoM formulation will be slightly different from the original one introduced previously (1.18). In fact, the impedance matrix **Z** will be separated in two contributions; the surface impedance and the substrate-related impedance contributions. The resulting MoM system of equations will be also implemented in Matlab and numerical simulations will allow validation of the code to open the way to a design procedure in Chapter 3.

2.1 MoM simulation of an already validated design

In this section, we analyze an already validated design found in the paper [18]. MoM simulations of the proposed antenna are carried out to obtain the currents from which we can compute the radiation pattern.

The metasurface antenna produced in the paper is visible in Fig. 2.1. The antenna is 1D, the sinusoidal surface impedance varies only along x and is given by

$$\eta_{surf}(x) = j\eta_0 X' \left[1 + M\cos\left(\frac{2\pi x}{a}\right)\right] \tag{2.1}$$

where X' is the average surface reactance normalized by the free-space wave impedance ($X' = X/\eta_0$), M the modulation factor and a the periodicity of the sinusoid. The main characteristics of the antenna radiating at 30° from broadside are listed in Table 2.1.

Table 2.1: The main characteristics of the antenna developed in reference [18].

Dimensions		**Dielectric substrate**		**Operating**	**Surface impedance** (2.1)		
Length	Width	Thickness	Permittivity ϵ_r	**Frequency**	M	X'	a
22.88 cm	3 cm	2.54 mm	6.15	10 GHz	0.2	1.2	28.25 mm

MoM simulations of the antenna are realized following the description given in Section 1.3.4 and based on the structure of the device and the parameters given in Table 2.1. The structure of the antenna is meshed using rooftop functions defined in the previous chapter and in Appendix A. These subdomain functions cover the surface of the antenna and allow to obtain numerical solution of currents.

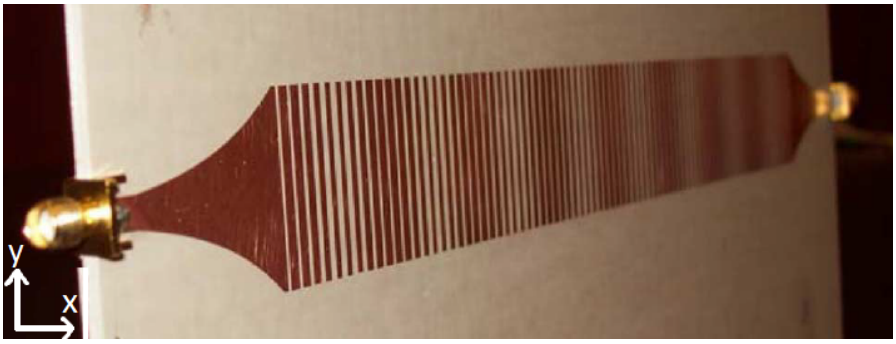

Figure 2.1: Leaky-wave antenna with a sinusoidally-modulated reactance surface from [18] with a 50Ω termination at one end.

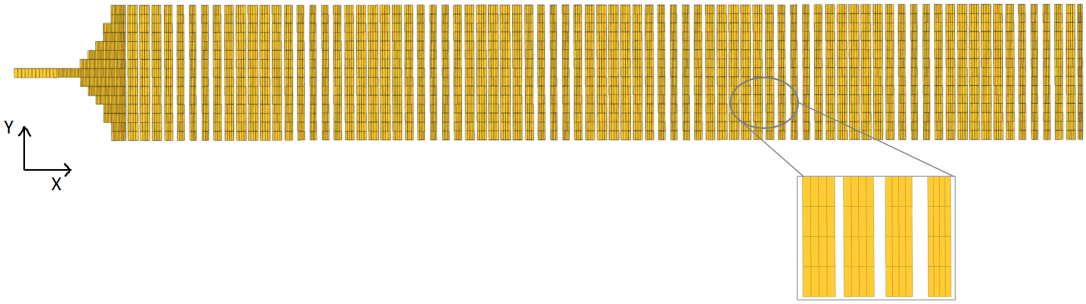

Figure 2.2: Antenna mesh for MoM simulation.

Fig. 2.2 shows the mesh corresponding to the simulated antenna. A Matlab code has been created to generate arbitrary meshes flexibly. The feed is represented close to reality and additional basis functions are added at the feed start to add a line of length $\lambda/4$ (short circuit).

Fig. 2.3 gives the radiation pattern in dB obtained through MoM simulation, as well as the pattern from the paper. We observe that the simulated pattern is very directive. Some characteristics, such as the width of the main beam and the presence of certain secondary lobes, are comparable with measurements. However, the pointing angle is not precisely 30°, a shift persists in the simulation (22.5° in Fig. 2.3(b)). Also, the directivity is 17.78 [dBi] compared to 18.4 [dBi] in the paper.

In addition to the shape of the pattern, it is interesting to analyze how the variation of specific parameters impacts it. This study will also validate the quality of MoM simulations. The paper highlights the influence of impedance parameters M and X' (see (2.1)), as well as the frequency. This will allow a comparison to simulations results. Table 2.2 compares RP principal pointing angle taken from the paper with the one calculated with the MoM code.

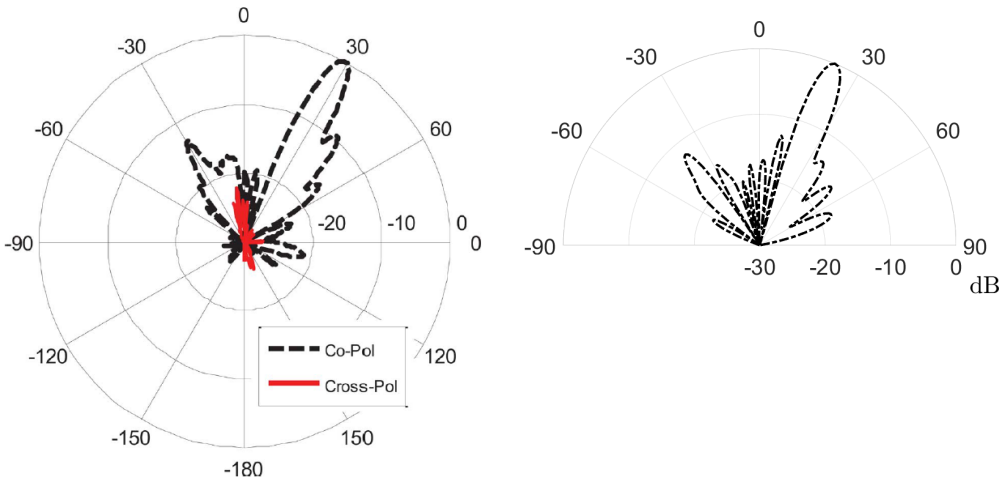

(a) Measured RP taken from the paper [18] (b) RP from MoM simulation

Figure 2.3: Radiation pattern $\mathbf{F}(\theta, \phi = \{90°, 270°\})$ of the antenna with sinusoidally-modulated reactance surface (2.1) from (a) measurements in the paper and (b) MoM simulation.

Table 2.2: (a) Influence of f $[GHz]$, (b) M and (c) X' on the main beam direction of the antenna resulting from the design described in the paper [18]. Results from the paper are transcribed and compared with those obtained through MoM simulation. Influence on the directivity is given for the MoM simulations in dBi.

	(a)			(b)			(c)		
	$f = 9$	$f = 10$	$f = 11$	$M = 0.1$	$M = 0.2$	$M = 0.4$	$X' = 1$	$X' = 1.2$	$X' = 1.4$
Pointing angle									
Measurement results from paper	13°	30°	48°	29.3°	30°	30.1°	×	×	×
Simulation MoM	5.625°	22.5°	40.5°	22.5°	22.5°	23.63°	15.75°	17.78°	31.5°
Directivity [dBi]									
MoM simulations	16.49	17.78	17.43	16.22	17.78	17.56	17.66	17.78	17.94

Measurements taken from the article indicate that increasing (decreasing) the frequency increases (decreases) the pointing angle. This described behaviour is also observed through simulations in Fig. 2.4(a). In Table 2.2(a), the shift angle due to frequency variation is the same for measurements and MoM simulation. Decreasing the frequency by 1 GHz amounts to reducing the angle by 17° and increasing it by 1 GHz to increase the angle by 18°.

Determining X' can help to design the beam direction. The article does not give any numerical values but indicates that when X' decreases (increases), the pointing angle decreases (increases). This behaviour is observed in the MoM simulation results in Fig. 2.4(c) and Table 2.2(c).

A third way to ensure the correct modelling of the antenna is to analyze the influence of M. Adjusting this parameter has no impact on the direction of the beam but allows the control of the width. This behaviour is once again demonstrated by simulations (Table 2.2(b) and Fig. 2.4(b)).

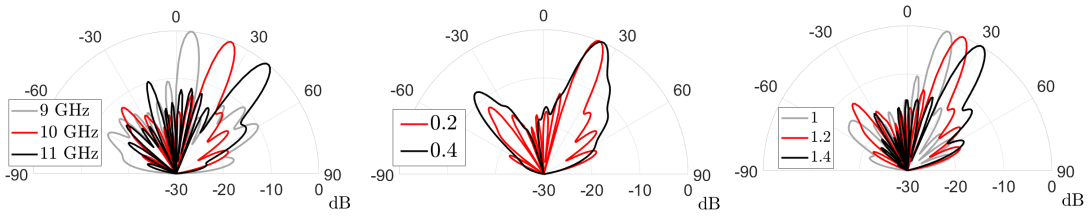

(a) Variation of f (b) Variation of M (c) Variation of X'

Figure 2.4: Variation of specfic parameters to observe the impact on the radiation pattern $\mathbf{F}(\theta, \phi = \{90°, 270°\})$ obtained by MoM simulation.

This first part of the analysis of 1D MTS antenna allowed MoM simulations from a known design validated in the reference paper. The impact of some parameters on the pattern are well modelled, but a beam squint remains present. This beam squint can come from accuracy errors in the mesh construction. Other potential errors can be caused by the presence of the feed or from its modeling.

2.2 Representation of the surface impedance in another basis

2.2.1 Principle

This section aims to solve the MoM problem by using entire basis and testing functions instead of subdomain functions. Fig. 2.5 summarizes the principle

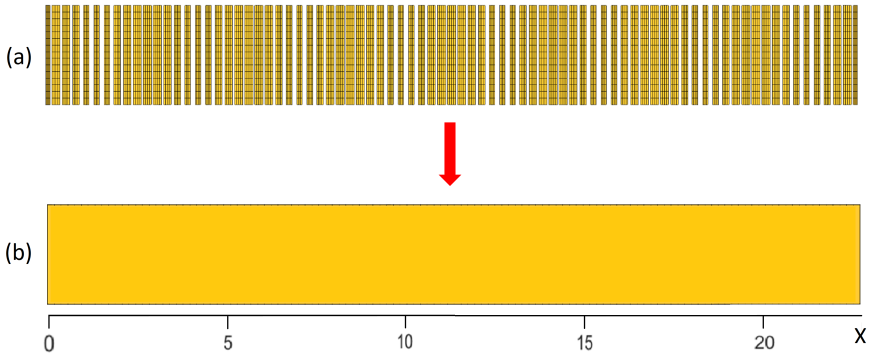

Figure 2.5: Basic principle behind the representation of the surface impedance in another basis. Scale is in [cm].

that interests us. The first structure, composed of patches meshed with rooftops, corresponds to the one simulated in the previous section from the reference [18].

The feed is discarded because we will not model it in the following of the thesis. Indeed, precise modelling of the feed is essential if one wants to know, for example, the input impedance of the antenna. However, this is not what interests us in this thesis because we focus only on the surface impedance of the antenna. In the following, we will suppose that the feed is a simple excitation. More information will be given on this approximation in the next section. Through MoM simulation, we have seen that it is possible to obtain the current distribution by using the discretized structure of the antenna with subdomains basis functions.

We would now like to use entire-domain basis functions to simulate the antenna's behaviour. It is possible starting from a simple structure, i.e. a rectangular patch covering the domain on which the antenna is defined. This is represented in the second configuration in the Fig. 2.5. On this unique patch, we will define a set of $2N+1$ entire-domain basis functions[1] $R_n(x)$ (with $n \in [-N:N]$). Those $R_n(x)$ will allow us to expand the sheet impedance, described by a continuous function, with pre-determined basis functions and therefore implementing the IBC. In the end, entire-domain basis functions will allow the rectangular patch to present the same surface impedance characteristics as the first structure composed of patches. However, N will be much lower than the number of rooftops meshing the first structure.

[1]All functions are constant along the y-direction (along the width) because we analyze 1D antenna.

2.2.2 Linear system to solve

This section describes the formulation of a new MoM problem which allows to simulate metasurfaces antennas with entire-domain functions $R_n(x)$.

The introduction of functions $R_n(x)$, different from rooftops functions, slightly modifies the linear MoM system of equations (1.18) and allows describing the substrate and the IBC (patches layer) impedance contributions separately [19]. We have

$$(\mathbf{Z_G} - \mathbf{Z_{IBC}})\,\mathbf{i} = \mathbf{v} \tag{2.2}$$

with $\mathbf{Z_G}$ and $\mathbf{Z_{IBC}}$ respectively the substrate and the IBC matrix contributions in the basis of $R_n(x)$ functions, $\mathbf{i}$ a vector describing the current distribution in $R_n(x)$ and $\mathbf{v}$ corresponds, within a minus sign, to the excitation fields onto the same functions. The explanation and calculation of each term will be detailed below.

$\mathbf{Z_G}$ is the contribution of the antenna substrate. This contribution does not change for a given operating frequency and substrate parameters (Table 2.1). As these last parameters will remain identical for the whole thesis, $\mathbf{Z_G}$ can therefore be calculated once and only once. In reality, we have

$$\mathbf{Z_G} = \mathbf{Q^T Z_{MoM} Q} \tag{2.3}$$

With $\mathbf{Z_{MoM}}$ a matrix obtained by MoM simulation of the rectangular patch (Fig. 2.5). This patch is simulated with the lab code because it already allows to take into account all the substrate's parameters. The rectangular patch is therefore meshed with a low number N_R of rooftops to obtain $\mathbf{Z_{MoM}}$, computed on the same basis. We must apply a basis change to obtain the matrix associated with basis and testing functions corresponding the the $R_n(x)$ functions. This basis change is made by evaluating each basis functions R_n at the top of the rooftops. This leads to a matrix $\mathbf{Q}$ of size $N \times N_R$. An example of such a projection is given in Fig. 2.6 with as $R_n(x)$ a sine function and the elements of the corresponding matrix Q are highlighted in red.

$\mathbf{Z_{IBC}}$, the contribution of the patches is computed as follows

$$Z_{IBC}(m,n) = \iint R_m(x) Z_S(x) R_n(x) dxdy \tag{2.4}$$

with $Z_S(x)$ the sheet impedance and $R_m(x), R_n(x)$ respectively the basis and testing functions. However, the impedance (2.1) provided in the paper corresponds to the **opaque impedance**. MTS structures can be represented as IBCs by opaque or sheet impedances. The first way consists in describing both the substrate and the upper layer (sheet) while the sheet impedance represents only the upper layer related to the patches. It is possible to extract the sheet impedance from the

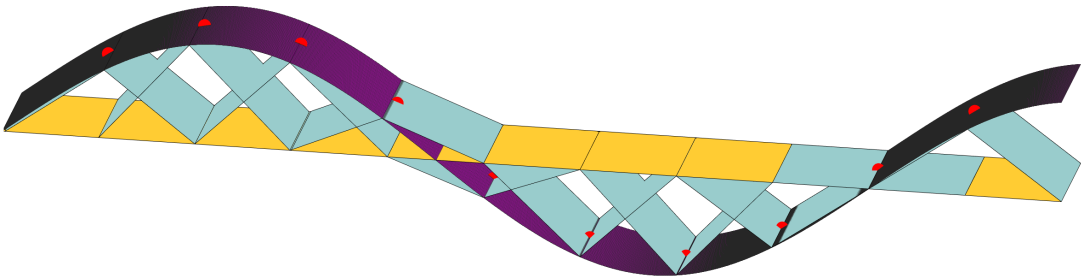

Figure 2.6: Example of the projection of rooftops functions (blue) on $R_n(x)$ function (purple). The obtained coefficients, at the top of the rooftops, are put in red.

opaque one. The developments to achieve this are provided in Appendix B. In this thesis, we work with the sheet impedance because this representation offers more accurate representation of the surface impedance and because we always work with the same substrate parameters.

Last element to discuss in (2.2) is $\mathbf{v}$, computed as follows

$$v(n) = -\iint R_n(x)E(x)dxdy \tag{2.5}$$

with $E(x)$ the excitation of the antenna. The excitation used in this thesis is given by

$$E(x) = \exp(-ik_{sw,slab}x) \tag{2.6}$$

where $k_{sw,slab}$ is the surface wavenumber in the substrate in the absence of the MTS. To obtain a leaky wave, the spectrum injected by the feed must contain the $k_{sw,slab}$ mode so that there is coupling with the metasurface. The excitation must correspond to the surface wave mode supported in the absence of MTS. By choosing the excitation (2.6), which is a surface wave propagating in the substrate without MTS, one excites exactly this mode.
The excitation of an infinite vertical dipole placed at the origin of the antenna (in $x = 0$ and middle of the width on the Fig. 2.5) was also tested. However, the results were non-conclusive. The spectrum of this excitation is much broader than the previous one; the power is shared between a higher number of modes. That would, therefore, not allow the $k_{sw,slab}$ mode to receive the power necessary to couple to the metasurface.

In the end, the system of equations (2.2) is solved to obtain the coefficients $\mathbf{i}$. Those coefficients allow to calculate the current distribution $J(x)$ along the antenna

in the basis of $R_n(x)$ functions:

$$J(x) = \sum_{n=-N}^{N} i_n R_n(x) \tag{2.7}$$

2.2.3 Choice of basis functions $R_n(x)$

The choice of the entire-basis functions $R_n(x)$ to solve the MoM system of linear equations (2.2) is important because it must meet a certain number of criteria which will be detailed in the following. The chosen entire-domain functions $R_n(x)$ are complex exponentials

$$R_n(x) = \exp\left(\frac{in2\pi}{a}x\right) \tag{2.8}$$

with a the length of the antenna. In this case, functions are defined on the whole domain of the unknown function $J(x)$, the current distribution. The domain is represented in Fig. 2.7(a). Integrations in (2.4) and (2.5) are realized on the whole surface of the antenna. One particularity of these functions is their periodicity and their equality in $x = 0$ and $x = a$ (at the beginning and end of the domain). This last constraint is therefore also applied to $J(x)$ reconstructed from these $R_n(x)$ in (2.7). Furthermore, these complex exponentials form a complete basis. That allows the reconstruction of any function in this base to converge with a reduced number N. That leads to a reduction in the solver's complexity, and a saving of time is also observed. Another property is that those functions, like their Fourier transform, are orthogonal. That property will prove to be very convenient when projections will need to be calculated in the following.

Once the system of linear equations (2.2) is solved with entire-domain functions, it is interesting to have a validation of the results. A validation means solving the system and computing the current distribution (2.7) again but by changing the basis functions $R_n(x)$. The choice of this second basis is none other than that of rooftops, which are purely real functions. Those functions are completely different from complex exponentials and will allow a good comparison of results.

Rooftop functions are defined based on notations from Fig. 1.6 as follows,

$$R_n(x) = \begin{cases} (x - x_{a_n})/(x_{b_n} - x_{a_n}), & x_{a_n} \leq x \leq x_{b_n} \\ (x_{c_n} - x)/(x_{c_n} - x_{b_n}), & x_{b_n} \leq x \leq x_{c_n} \\ 0, & else \end{cases} \tag{2.9}$$

As already explained, rooftops are subdomain basis functions. Therefore, the definition domain of the antenna must be discretized (see Fig. 2.7(b)). The number

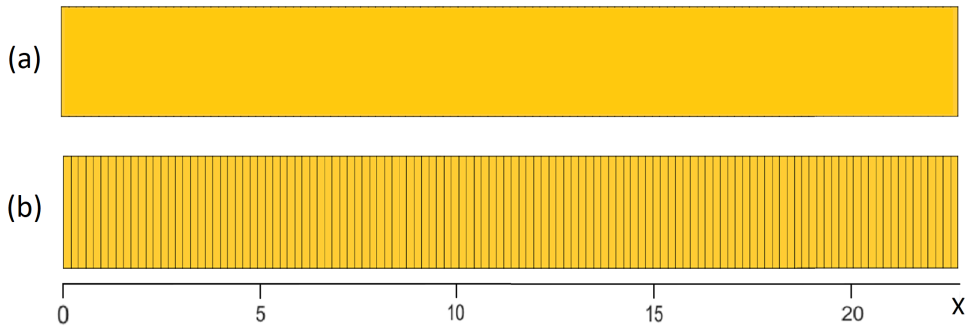

Figure 2.7: (a) Definition domain for the complex exponentials (entire-domain functions) (b) Discretization of the whole domain by rooftops functions (subdomain functions). Scale is in [cm].

of basis functions will be more important than that of complex exponentials. In fact, in the following we will consider 571 rooftops compared to only maximum 250 complex exponentials. With rooftops, there is no need to calculate the matrix projection $\mathbf{Q}$ in (2.3) and integrations in (2.4) and (2.5) are carried out on the definition domain of a single rooftop basis function.

MoM simulations will therefore be carried out using complex exponential functions and rooftops. If the solution of the system of equations (2.2) obtained in the two bases are consistent, the current distribution $J(x)$ is indeed correct. In the following, the use of rooftop basis functions will only be useful as a validation step.

2.2.4 Numerical simulations

For the simulations carried out in this section, we always consider the design realized in reference [18]. We consider parameters from Table 2.1 as well as the sheet impedance extracted from the analytical expression (2.1).

Solving the system of equations (2.2) using the two basis functions described in Section 2.2.3 results in current distributions $J(x)$. From those currents, one can compute the patterns shown in Fig. 2.8. We note that the two patterns are essentially identical. The solution from entire-domain functions $R_n(x)$ is validated from the one obtained with rooftops. We can look at main characteristics given in Table 2.3. Despite a slight decrease in directivity due to higher sidelobes, values are similar to those obtained previously through MoM simulation with the lab code in Section 2.1.

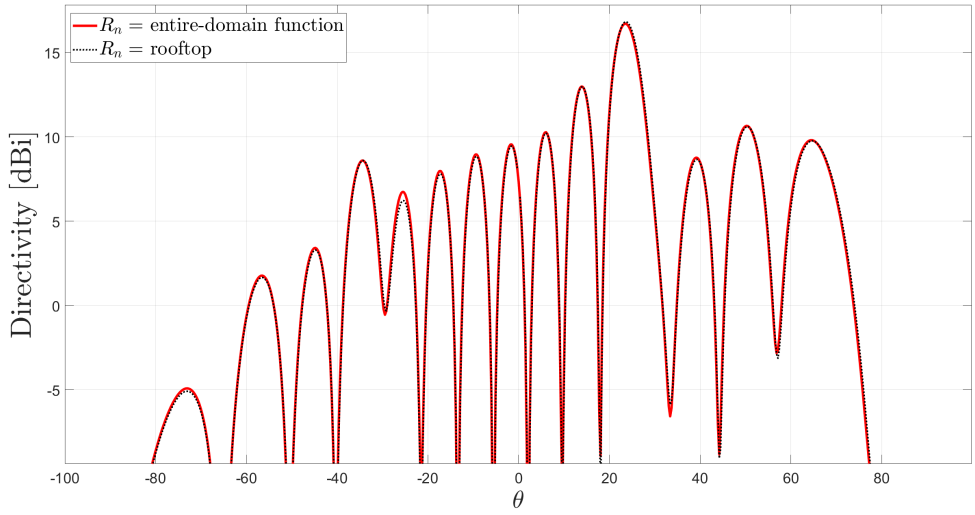

Figure 2.8: Directivity obtained following the solution of system (2.2) with two kinds of basis functions (rooftops and complex exponentials).

Table 2.3: Summary of results following numerical simulations from the known opaque impedance (2.1).

	R_n =rooftop	$R_n = \exp(in2\pi x/a)$	MoM simulation
Angle main beam [°]	23.45	23.45	22.5
Directivity [dBi]	16.83	16.72	17.78

A final modification is made to the simulations. Until now, the sheet impedance ($Z_S(x)$ in equation (2.4)) was extracted from the opaque impedance (2.1) referenced in the paper. That can introduce approximations. Then, it is more efficient to work directly with an analytical expression of the sheet impedance. From now on, the following formula for the sheet impedance, taken from the literature, is used

$$Z_S(x) = Z_{S0}(1 + (M \sin(k_{sw}x - k_0 x \sin\theta_0))) \tag{2.10}$$

with k_{sw} the wavenumber of the surface wave used to excite the antenna, Z_{S0} the mean value and θ_0 the desired angle of radiation. We can, based on (2.10) better understand how a LW antenna radiates following the interaction between the patches and the surface wave (SW). We have seen in Section 1.1.2 and more precisely on the Fig. 1.4 that a LW antenna radiates when a spatial harmonic falls in the visible region of the spectrum. These harmonics are related to the SW wavenumber k_{sw} and are produced in presence of a periodic pattern, defined through the sinusoidally-modulated sheet impedance (2.10). They are defined as

follows

$$k_{xn} = k_{sw} + \frac{2\pi n}{p} \quad \forall n \in \mathbb{Z} \tag{2.11}$$

with p the periodicity of the sheet impedance modulation and k_{xn} the tangential wave number of the nth spatial harmonic. A LW antenna radiates at a desired angle θ_n if the following condition is verified (see Fig. 2.9)

$$\sin(\theta_n) = \frac{k_{xn}}{k_0} \Longrightarrow |k_{xn}| \leq k_0 \tag{2.12}$$

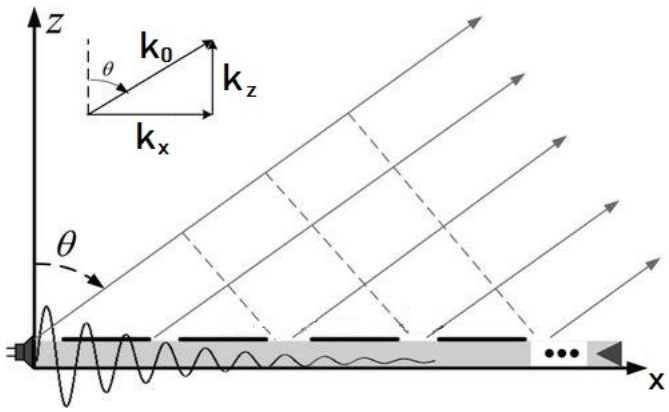

Figure 2.9: Schematic representation of a leaky-wave structure [20]

By combining (2.11) with (2.12) we obtain the following condition that must be verified by the harmonics in order to radiate

$$|k_{sw} + \frac{2\pi n}{p}| \leq k_0 \tag{2.13}$$

We know that the SW does not verify (2.12) because it is an evanescent wave. Since this wave does not radiate, we have $|k_{sw}| > k_0$. From this observation and (2.13), we can find a condition on n for the radiating harmonics

$$\frac{2\pi n}{p} < 0 \Longrightarrow n < 0 \tag{2.14}$$

In general, it is the radiation harmonic -1 which radiates. Therefore, the desired radiation angle can be defined for this radiating spatial harmonic by combining (2.11) and (2.12) for $n = -1$

$$k_0 \sin(\theta_{n=-1}) = k_{sw} - \frac{2\pi}{p} \tag{2.15}$$

We observe that the modulation of the sheet impedance (2.10) is directly related to the radiation angle $\theta_{n=-1}$ of the radiating -1 harmonic (2.15) as follows

$$M \sin\left(\frac{2\pi x}{p}\right) = M \sin\left(k_{sw} x + k_0 x \sin\left(\theta_{n=-1}\right)\right) \tag{2.16}$$

Through these developments we highlight the fact that it is the surface impedance which partially transforms the surface wave that does not radiate into a leakage wave, through the creation of harmonics.

The sheet impedance (2.10) is used for simulations with the radiation angle $\theta_{n=-1}$ equal to 30° to respect the design from the reference paper [18]. When using directly the analytical expression of the sheet impedance, we obtain by simulation a pattern pointing at 27.06° with a directivity of 16.62 dBi. Compared to results obtained starting from the opaque impedance (see Table 2.3), we trade a little directivity to be closer to the desired 30°.

At the end of this chapter, we can conclude that results obtained with entire-domain basis functions in this section are consistent with the first MoM simulations realized with the laboratory code in Section 2.1. These performances validate the implementation and solution of the new system of equations allowing the distinction between substrate and sheet impedance contributions (2.2). Based on this good news, we will be able to synthesize the design procedure.

Chapter 3

Synthesis of 1D modulated metasurface antennas

This chapter presents a method to design 1D MTS antennas. The principle is to derive the surface impedance, which makes it possible to obtain the desired radiation pattern, assuming that the excitation of the MTS is known a priori. That corresponds to the solution of a problem that is reciprocal to the one discussed so far. In the previous chapter, we have solved the system of equations (2.2) to determine the currents from a known impedance surface. From now on, the current distribution is known and will allow the determination of the surface impedance. This is what we will call the inverse problem.

In the following sections, we will explore the design procedure. First of all, the formulation of the inverse problem is presented, and some new notations are introduced. Then, some essential steps will be developed, such as calculating the desired current distribution or the least-squares solution of the problem. Finally, numerical simulations will validate the implementation of the synthesis procedure.

Before entering in too much detail, it is essential to remember that this thesis deals with a 1D antenna. Therefore, all the quantities only depend on the position along the antenna. Consequently we seek to determine $Z_S(x)$.

3.1 Inverse problem formulation

The surface impedance is constrained to be purely imaginary to avoid losses on the sheet and is defined as the sum of an average value and a modulation.

$$Z_S(x) = jX_0 + P(x) \tag{3.1}$$

To formulate the inverse problem from (2.2) and determine $Z_S(x)$, it is necessary to decompose this surface impedance in the basis of $R_n(x)$ functions introduced in

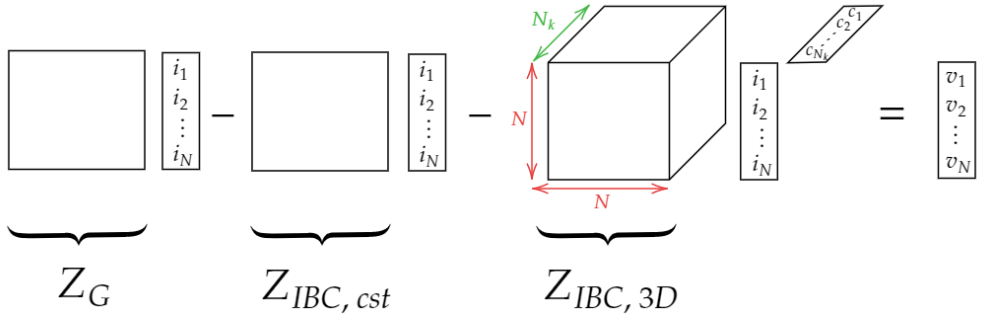

Figure 3.1: Schematic representation of the formulation of the inverse problem.

the Chapter 2. The number of functions used to represent the impedance is not necessarily equal to that of the basis and testing functions used previously for the current, equal to $2N + 1$ (see (2.7)). We consider here $2N_k + 1$ functions noted $R_k(x)$. We can expand the surface impedance with those functions as follows

$$Z_S(x) = jX_0 + \sum_{k=-N_k}^{N_k} c_k R_k(x) \tag{3.2}$$

By introducing (3.2) in the expression of Z_{IBC} (2.4) we obtain the following expression

$$Z_{IBC,inv}(m,n) = \underbrace{j \iint R_m(x) X_0 R_n(x) dxdy}_{Z_{IBC,cst}(m,n)} + \sum_{k=-N_k}^{N_k} c_k \underbrace{\iint R_m(x) R_k(x) R_n(x) dxdy}_{Z_{IBC,3D}(m,n,k)} \tag{3.3}$$

Expression (3.3) contains a 3D matrix due to the new decomposition of the impedance. The MoM system of equations (2.2) is modified accordingly

$$\mathbf{Z_G i} - \mathbf{Z_{IBC,cst} i} - \sum_{k=-N_k}^{N_k} c_k \mathbf{Z_{IBC,3D} i} = \mathbf{v} \tag{3.4}$$

A schematic representation of the formulation of the inverse problem can be found in Fig. 3.1. As explained earlier, currents are known for the design procedure. Their calculation will be explained in the next section but here we assume they are completely determined. Therefore, we can reduce the 3D matrix $\mathbf{Z_{IBC,3D}(m,n,k)}$ by multiplying it with the vector of currents $\mathbf{i}$. This yields to the inverse problem formulation, represented in Fig. 3.2. The analytical expression is given by

$$\mathbf{Z_G i} - \mathbf{Z_{IBC,cst} i} - \mathbf{Z_{IBC,2D} c} = \mathbf{v} \tag{3.5}$$

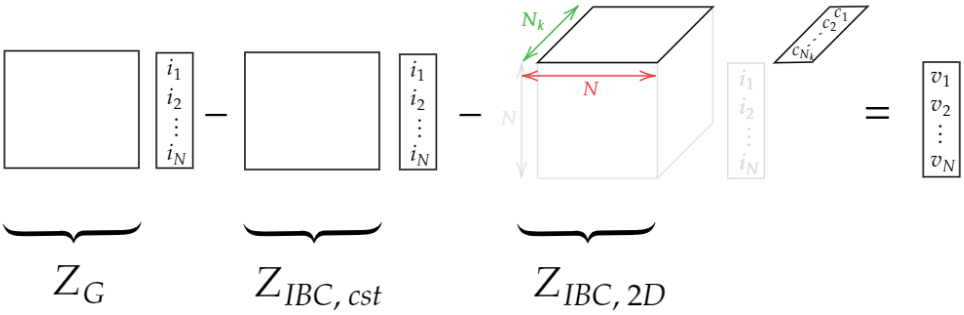

Figure 3.2: Schematic representation of the reduced inverse problem.

where $\mathbf{c}$ are the new parameters to compute in order to obtain the surface impedance (3.2).

In the following sections, the design method is implemented with the entire-domain basis function $R_n(x) = \exp\left(\frac{in2\pi}{a}x\right)$, which allows working in the spectral domain because their Fourier transforms are orthogonal. However, the entire procedure is also implemented using rooftops to enable the validation of the results with the use of different basis functions. Unfortunately, Fourier transforms of rooftops are not orthogonal and one must slightly adapt the algorithm. We will briefly discuss the necessary adjustments in Section 3.2.3 dedicated especially to the resolution of (3.5) with rooftops.

3.2 Inverse problem solution

3.2.1 Current calculation

We have already explained previously that for the design procedure, the currents are known. This section explains how they are obtained.

In the inverse problem (3.5), part of the known currents $\mathbf{i}$ is calculated from the desired initial pattern. This radiation pattern in spectral domain $\mathbf{F_{init}}(k_x, k_y)$ is the desired quantity we choose at the beginning of the design procedure. We define it in amplitude and phase within a constant multiplicative factor, which depends on the radiated power of the antenna [8]. In this thesis, $\mathbf{F_{init}}$ is purely transverse magnetic (TM) because we are facing a 1D situation where the polarization is limited by construction to the TM case ($\mathbf{F_{init,TE}} = 0$). Moreover, one cannot control the variations of the spectral quantities along k_y. We will assume that the fields are invariant in translation along the y coordinate. In the following, all the spectra will be considered purely TM and analyzed exclusively in the plane $k_y = 0$. They will be assumed as dependent on k_x only. We introduce this notation for

more clarity

$$\mathbf{F_{init}}(k_x) = \mathbf{F_{init,TM}}(k_x, k_y = 0) \tag{3.6}$$

The far-field pattern $\mathbf{F_{init}}(k_x)$, for antenna applications, only allows calculating the visible contribution of currents. On the other hand, fields close to the surface of the antenna determine the invisible currents. This invisible contribution can be computed based on the unmodulated impedance. The total desired current is the sum of the rescaled visible current with respect to the radiated power and the invisible currents:

$$\mathbf{i} = A\mathbf{i_{vis}} + \mathbf{i_{inv}} \tag{3.7}$$

with A the rescaling factor. In this section, we will first go through the calculation of the visible currents, and then we will move on to the invisible one. Notions of visible and invisible currents were introduced in Section 1.1.2.

Visible current

In the purely TM case, equations (1.6) and (1.7) are simplified. We can inverse those relations to obtain directly, in spectral domain:

$$\mathbf{F_{init}}\left(k_x\right) = \widetilde{\mathbf{E}}\left(k_x\right) \tag{3.8}$$

With this equality, we observe that we determine $\widetilde{\mathbf{E}}$, the visible spectrum of the aperture tangential electric field, directly by imposing the desired pattern. Using equation (1.4) and the dyadic spectral Green's function associated with the substrate $\widetilde{\mathbf{G}}\left(k_x\right)$, we can compute the visible spectral current distribution on the MTS antenna.

$$\widetilde{\mathbf{J}}_{vis}\left(k_x\right) = \frac{\widetilde{\mathbf{E}}\left(k_x\right)}{\widetilde{\mathbf{G}}\left(k_x\right)} \tag{3.9}$$

Projection of this distribution on the set of N basis function $R_n(x)$ allows to obtain coefficients $\mathbf{i_{vis}}$ in the same basis.

$$\int_{-k_0}^{k_0}\int_{-k_0}^{k_0} \widetilde{R}_n^{\star}\left(k_x\right)\widetilde{\mathbf{J}}_{vis}\left(k_x\right)dk_xdk_y = \int_{-k_0}^{k_0}\int_{-k_0}^{k_0} i_{n,vis}\widetilde{R}_n^{\star}\left(k_x\right)\widetilde{R}_n\left(k_x\right)dk_xdk_y \tag{3.10}$$

$$i_{n,vis} = \frac{\int_{-k_0}^{k_0}\int_{-k_0}^{k_0} \widetilde{R}_n^{\star}\left(k_x\right)\widetilde{\mathbf{J}}\left(k_x\right)dk_xdk_y}{\int_{-k_0}^{k_0}\int_{-k_0}^{k_0} \widetilde{R}_n^{\star}\left(k_x\right)\widetilde{R}_n\left(k_x\right)dk_xdk_y} \tag{3.11}$$

for $n \in [-N; N]$ and integrations over the visible spectrum.
These currents are given up to a constant A. This constant is related to power radiated from the antenna as follows

$$A = \sqrt{\frac{lP_{desired}}{P_{radiated}}} \tag{3.12}$$

with $P_{radiated}$ computed from (1.10) where the fields are obtained from the visible currents, directly computed from the pattern. $P_{desired}$ can be estimated first by computing the power radiated from the unmodulated impedance, that is jX_0 from (3.2). Remember that the unmodulated impedance supports only the surface wave, which does not radiate. The power which is obtained is therefore not significant. This estimated power value can be slightly tuned through the constant l to optimize the design.

Invisible current

As a reminder, the invisible currents are those that don't contribute to the far-field radiation pattern. They are simply obtained from the unmodulated impedance. Those currents are computed in the basis of $R_n(x)$ functions and their visible part is filtered in spectral domain. Spectral currents are then re-projected using (3.10) to obtain coefficients $\mathbf{i_{inv}}$.
It is essential to mention that calculating the invisible currents from the unmodulated impedance is an approximation. Indeed, that imposes to take into account only one mode in the invisible spectrum whereas, in reality, other harmonics are present (see Fig. 1.4).

In Fig. 3.3 are represented the different spectral currents contributions obtained from a desired pattern with a pencil beam pointing at 30°. The design is simulated at 10 GHz considering the substrate parameters given in Table 2.1. In this figure are given the rescaled visible currents $\widetilde{\mathbf{J}}_{\mathbf{vis,rescaled}}(k_x)$, the invisible currents $\widetilde{\mathbf{J}}_{\mathbf{inv}}(k_x)$ and the sum of both $\widetilde{\mathbf{J}}(k_x)$. The spectral domain is normalized by k_0 so that the invisible part is defined for $k_x/k_0 > 1$. In the cut of the total spectral currents for $k_y = 0$ we observe the presence of the SW mode ($k_{sw}/k_0 = 1.56$) in the invisible region.

3.2.2 Least-squares solution

Now that we have the desired currents, one can reduce the 3D matrix as explained in Section 3.1 to obtain the system of equations (3.5) and solve for coefficients $\mathbf{c}$.

$$\mathbf{c} = \left(\mathbf{Z_{IBC,2D}}\right)^{-1} \mathbf{Z_G i} - \mathbf{v} - \mathbf{Z_{IBC,cst} i} \tag{3.13}$$

These coefficients will then allow us to obtain the surface impedance (3.2). To resolve the system of equations, we have to impose a constraint about the purely imaginary character of the surface impedance. Otherwise, it means there are losses in the structure. To impose the modulation part $\sum_{k=-N_k}^{N_k} c_k R_k(x)$ to be imaginary we have the following condition to respect, knowing that $R_k(x) = \exp\left(\frac{in2\pi}{a}x\right)$ is

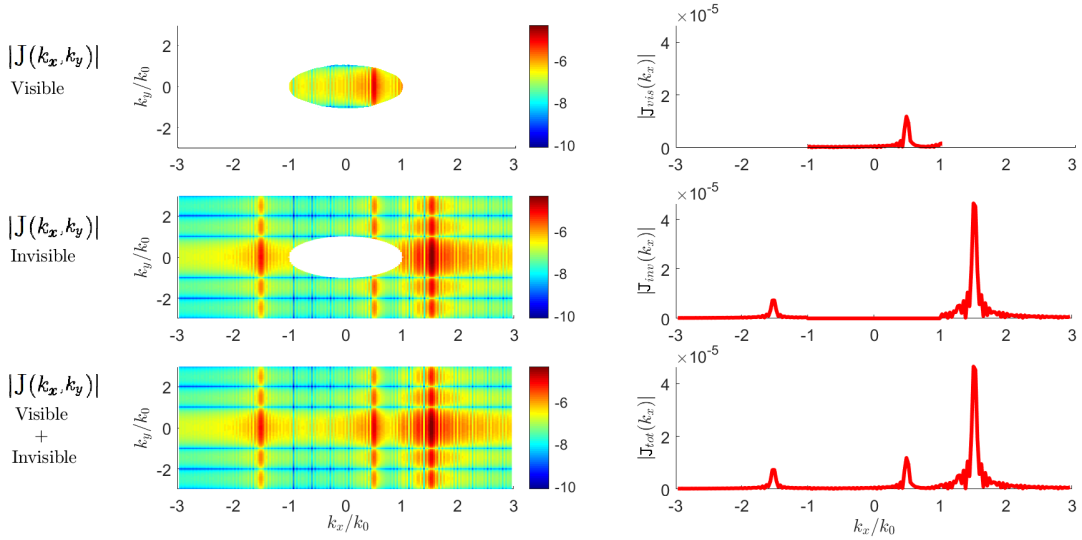

Figure 3.3: From top to bottom we have successively the spectrum of visible rescaled currents, the spectrum of invisible currents and the spectrum of the sum of both contributions. Those spectra are given on the left in the (k_x, k_y) plane normalized by k_0 and on the right for a cut of the plane in $k_y/k_0 = 0$.

purely imaginary.

$$c_k = -c^{\star}_{-k} \tag{3.14}$$

However, it is possible to impose the constraint differently so that it is easier to implement numerically. For that, a basis change is made to work with real basis functions. This basis change is the following

$$R'_k(x) = \begin{cases} \frac{R_k(x)+R_k(-x)}{2} = \cos\left(\frac{n2\pi}{a}x\right), & \text{for } n \geq 0 \\ \frac{R_k(x)-R_k(-x)}{2} = \sin\left(\frac{n2\pi}{a}x\right), & \text{for } n < 0 \end{cases}$$

The surface impedance described in this new basis using sine and cosine functions corresponds to a Fourier decomposition.

$$Z_S(x) = jX_0 + \sum_{k=-N_k}^{N_k} c_k R'_k(x) \tag{3.15}$$

Basis functions $R'_k(x)$ are now real functions. Therefore, to constrain the modulation part $\sum_{k=-N_k}^{N_k} c_k R'_k(x)$ to be imaginary we simply have to impose all the c_{n_k} to be purely imaginary. This constraint leads to the least-squares solution of the system

of linear equations (3.5). This system is rewritten for clarity as follows

$$\begin{aligned} &\mathbf{Ax} = \mathbf{b} \\ \text{with } &\mathbf{A} = \mathbf{Z_{IBC,2D}} \\ &\mathbf{x} = \mathbf{c} \\ &\mathbf{b} = \mathbf{Z_G i} - \mathbf{v} - \mathbf{Z_{IBC,cst} i} \end{aligned} \tag{3.16}$$

Expanding real and imaginary terms of (3.16) leads to a system of 2 equations

$$\begin{cases} \mathbb{R}(\mathbf{A})\,\mathbb{R}(\mathbf{x}) - \mathbb{I}(\mathbf{A})\,\mathbb{I}(\mathbf{x}) = \mathbb{R}(\mathbf{X}) \\ \mathbb{R}(\mathbf{x})\,\mathbb{I}(\mathbf{A}) + \mathbb{R}(\mathbf{A})\,\mathbb{I}(\mathbf{x}) = \mathbb{I}(\mathbf{b}) \end{cases}$$

Knowing that all the c_k are purely imaginary, we can apply the constraint $\mathbb{R}(\mathbf{x}) = 0$ to obtain a system of 2 equations and 1 unknown

$$\begin{bmatrix} -\mathbb{I}(\mathbf{A}) \\ \mathbb{R}(\mathbf{A}) \end{bmatrix} \mathbb{I}(\mathbf{x}) = \begin{bmatrix} \mathbb{R}(\mathbf{b}) \\ \mathbb{I}(\mathbf{b}) \end{bmatrix}; \tag{3.17}$$

The resulting least-squares solution $\mathbb{I}(\mathbf{x})$ is the imaginary part of all the coefficients we have to determine ($\mathbb{I}(\mathbf{x}) = \mathbb{I}(c_k)$). The purely imaginary surface impedance can be reconstructed as follows

$$\underbrace{Z_S(x)}_{\text{imaginary}} = j\,\underbrace{X_0}_{\text{real}} + \sum_{k=-N_k}^{N_k} j\,\underbrace{\mathbb{I}(c_k)\,R'_k(x)}_{\text{real}} \tag{3.18}$$

We have therefore determined the surface impedance $Z_S(x)$, which, coupled with the surface wave, makes it possible to radiate the desired pattern.

3.2.3 Adaptation of the design procedure to rooftops basis functions

The previous sections describe the design procedure using the entire-domain basis functions (2.8). It is also possible to implement it with our second type of functions, the rooftops (2.9) for validation purposes. However, this requires some adjustments and those will be briefly explained here. Indeed, we can't perform projections such as (3.11) using rooftops because their Fourier transforms are not orthogonal. We must therefore compute the visible and invisible currents in the spatial domain.

Visible current

We must first bring the spectrum of desired visible currents (3.9) in the spatial domain to compute the visible current distribution $J_{vis}(x)$. We therefore apply an inverse Fourier Transform

$$J_{vis}(x) = \mathrm{IFT}\{\widetilde{\mathbf{J}}_{\mathbf{vis}}(k_x)\} \tag{3.19}$$

Then, the current distribution is evaluated at the centre of the rooftops to obtain desired visible currents in this same basis.

$$\mathbf{i_{vis}} = J_{vis}(x = \text{centre}_{\text{rooftops}}) \tag{3.20}$$

This calculation amounts to calculating the projection illustrated in Fig. 2.6 where the sine wave is $J_{vis}(x)$ and the red points the resulting coefficients $\mathbf{i_{vis}}$. The calculation of the rescaling factor A remains identical to (3.12).

Invisible current

The calculation of invisible currents is identical to that of visible currents, except that $\widetilde{\mathbf{J}}_{\mathbf{inv}}(k_x)$ is derived from the unmodulated impedance. In addition, the invisible part of the spectrum is filtered.

$$J_{inv}(x) = \text{IFT}\{\widetilde{\mathbf{J}}_{\mathbf{inv}}(k_x)\} \tag{3.21}$$

We also recover the currents after projection on rooftops.

$$\mathbf{i_{inv}} = J_{inv}(x = \text{centre}_{\text{rooftops}}) \tag{3.22}$$

Least squares solution

The solution is similar to the one presented in Section 3.2.2. However, the basis change is not necessary because rooftops are already purely real functions.

3.2.4 Design algorithm

The design algorithm discussed in previous sections is summarized in Fig. 3.4. The green boxes represent the inputs of the procedure and the red one the output, which is the surface impedance. Among the inputs we have

- the initial desired pattern $\mathbf{F_{init}}(k_x)$
- the average sheet impedance X_0
- the impedance matrix of the substrate Z_G (2.3)
- the excitation vector $\mathbf{v}$ known a priori

Rescaled visible and invisible currents are obtained from the initial pattern and the average sheet impedance. Their sum contributes to the reduction of the 3D IBC matrix by one dimension. Finally, the obtained 2D matrix takes part in a

system of equations (3.16) one can resolve in the least-squares sense to compute the surface impedance $Z_S(x)$.

The circled elements of the diagram represent the three radiation patterns calculated during the design process. These patterns will be at the basis of the simulation analysis in the next section. It is useful to recall what they represent.

- $\mathbf{F_{init}}(k_x)$ corresponds to the input of the algorithm, equivalent to the visible spectrum of the aperture tangential electric field (3.8).
- $\mathbf{F_{desired}}(k_x)$ is the pattern calculated from the desired currents. Ideally, we should have
$$\mathbf{F_{init}}\left(k_x\right) = \mathbf{F_{desired}}\left(k_x\right) \tag{3.23}$$
However, this will not be verified in the simulations. The projections into the $\widetilde{R}_n(x)$ basis to calculate the currents introduce approximations. Those functions being cardinal sines, the pattern $\mathbf{F_{desired}}$ will therefore be a version of the ideal pattern $\mathbf{F_{init}}$ presenting sidelobes.
- $\mathbf{F_{design}}(k_x)$ is the pattern simulated from the known surface impedance obtained by least-squares solution (3.18).

A good design consists of obtaining $\mathbf{F_{design}}(k_x)$ as close as possible to $\mathbf{F_{desired}}(k_x)$. The directivity extracted from those patterns as well as the input $\mathbf{F_{init}}(k_x)$ of the system will be compared and analyzed through numerical simulations in Section 3.3.

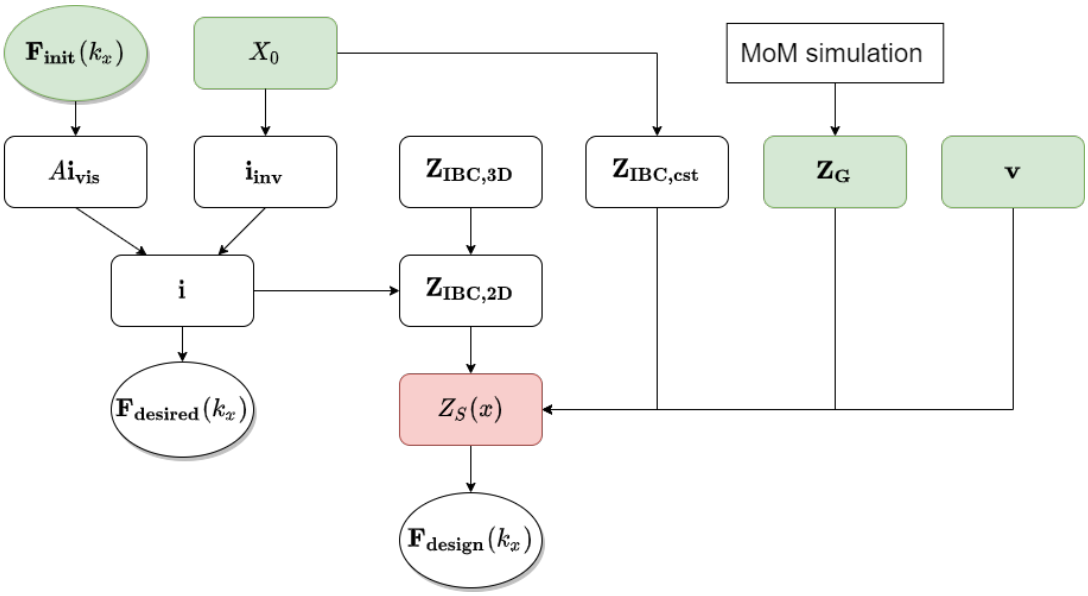

Figure 3.4: Summary of the algorithm for IBC computation.

3.3 Numerical simulations

In this section, different designs are presented. The inverse problem is applied to different types of desired patterns; a pencil beam, multibeams and a flat top beam. These patterns have different characteristics allowing the analysis of the performance of the design procedure. It is essential to specify that the design method imposes a constraint on the type of pattern that can be designed. A very wide pattern (which results in low directivity) is complicated to achieve. Indeed, the design will be limited by the spatial flexibility available to implement the necessary surface impedance able to transform the surface wave into leaky wave. In other words, the antenna must support a surface impedance allowing fine enough control over the surface wave to radiate in the desired directions.

The whole procedure and simulations are carried out using the set of entire-domain basis functions (complex exponentials (2.8)) and then validated with rooftops. Since the results in the two bases are consistent, only those obtained from the first type of functions will be displayed for better readability. The only thing that differs in the use of these two functions is the simulation time. As already discussed, using rooftops increase the number of needed basis functions and, therefore, the complexity of the algorithms. For example, to synthesize the surface impedance for a pencil beam pattern, simulation time with rooftops is around 153 seconds compared to only 19 seconds with entire-domain basis functions. However, it should be noted that the system of equations resulting from subdomain functions is sparse unlike that resulting from entire-domain functions.

3.3.1 Optimization of the design

To optimize the design we can tune four parameters of the algorithm.

1) The number of basis and testing functions N ***and IBC expansion functions*** N_k***.***
Sometimes there is a need to modify the number of basis functions to reduce the error due to different projections. We can generally consider for rooftop functions 10 functions per wavelength and that can be less for entire-domain functions. With the experience acquired during the simulations we note that the number of functions N is more important than the number N_k of expansion functions.

2) Estimated power.
Through the parameter l (3.12) one can tune the desired power previously estimated from the unmodulated impedance. This parameter, therefore, influences the rescaling factor A, which in turn makes it possible to modify the balance between

the visible and invisible currents.

3) Antenna length.
One can intuitively analyze the impact of the antenna length on the radiated pattern.
Let us take the example of an antenna of finite length whose fields on the aperture are constant. We know that the fields are related to the radiation pattern through the Fourier transform (1.6). Taking the Fourier transform of the constant fields results in a cardinal sine function in spectral domain. As a result, the radiation pattern exhibits sidelobes and maximum directivity in the direction of the main beam.
If we now consider the limit case of an antenna of infinite length, the radiation pattern is a simple Dirac delta function. This delta implies infinite directivity in a particular direction.
Intuitively, we notice that increasing the length of the antenna can possibly increases the directivity.

4) Linear phase shift applied to the initial pattern.
As a reminder, we define $\mathbf{F_{init}}(k_x)$ in amplitude and phase

$$\mathbf{F_{init}}(k_x) = |\mathbf{F_{init}}(k_x)|e^{-ik_x s} \tag{3.24}$$

with s the shift factor. Multiplying the pattern by a complex exponential allows for shifting the fields in the spatial domain. It is interesting to intuitively analyze the impact that this phase shift has on the antenna's radiation.
Fig. 3.5 represents a MTS antenna, the feed excitation to its left and two different field distributions.
Configuration 1 (in blue color) shows an evolution of the fields, which imposes very little radiation along the antenna to finally release all the power at the opposite end of the feed. Unfortunately, for physical reasons, this kind of behaviour is very complicated to achieve in practice.
The configuration 2 (a shifted version of previous case), on the other hand, leads to a more realistic interpretation of the evolution of the fields. The configuration requires the majority of power to be radiated at the centre of the antenna.
Thus, the complex exponential applied to the pattern allows the adaptation of the fields to make the system physically interpretable and feasible.

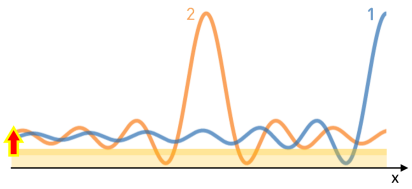

Figure 3.5: Schematic representation of the radiated fields influenced by the linear phase shift applied to the radiation pattern. The excitation is represented by an arrow.

More attention will be paid to the last two parameters in the following.

Before moving on to numerical simulations, it is essential to remember that all the designs are realized at 10 GHz. Also, Table 2.1 references all parameters of the simulations relating to the substrate or initial dimensions of the antenna. The average sheet reactance used is $X_0 = 340.5\ \Omega$. This value is extracted from the mean opaque impedance described by (2.1).

3.3.2 Pencil beam

This section considers the design of a pencil beam pointing in the range $[28.7°; 31.3°]$ (elevation angles). We start by analyzing the impact of the length of the antenna on the pattern considering no linear phase shift applied to $\mathbf{F_{init}}$. In Fig. 3.6 we observe that by doubling the length of the antenna, we go from a maximum directivity of 16.35 dBi to 20.5 dBi. In addition, the general appearance of the pattern after design (solid line) is more compliant with that of the desired pattern (dotted line). The width of the main beam is smaller. These observations confirm the intuitive analysis discussed in Section 3.3.1. Doubling the length of the antenna leads to better results. We will keep this modification for the following. In Fig. 3.6 we also notice the presence of an important backlobe in -30° (k_x/k_0 = -0.5). It is a secondary lobe pointing in the opposite direction to the desired one. It is certainly due to the reflection that occurs at the end of the antenna.

The influence of the linear phase (3.24) is visible in Fig. 3.7. We can observe the designed patterns for the shift factor s equal to 0, 10 and 30. Increasing the shift factor allows increasing the directivity from 20.5 dBi to 22.03 dBi. Shifting the fields along the antenna improves the results, but the impact is not considerable. It will be much more interesting to analyze the impact of the linear phase in the case of the flat top beam, in Section 3.3.4.

Based on the previous observations, we can validate the design obtained by doubling the antenna length and dephasing the desired pattern using the phase factor $e^{-ik_x 30}$. The obtained radiation pattern is given in green in Fig. 3.7. The corresponding $\mathbf{F_{init}}(k_x)$, $\mathbf{F_{desired}}(k_x)$ and $\mathbf{F_{design}}(k_x)$ patterns are given in Appendix C.1. One can also have a look at the surface impedance $Z_S(x)$, current distribution $J(x)$ and evolution of the electric field along the antenna. Those quantities are visible in Fig 3.8. The electric field must be analyzed because it is necessary to observe its decrease along the antenna. Ideally, at the end of the structure, the power must be totally radiated to avoid reflections.

The surface impedance is purely imaginary and is modulated around the average value X_0, as expected. The current density follows the same modulation period as the impedance and slightly decreases along the antenna. That appears quite logical, the current decreasing following the radiation. The same remark can

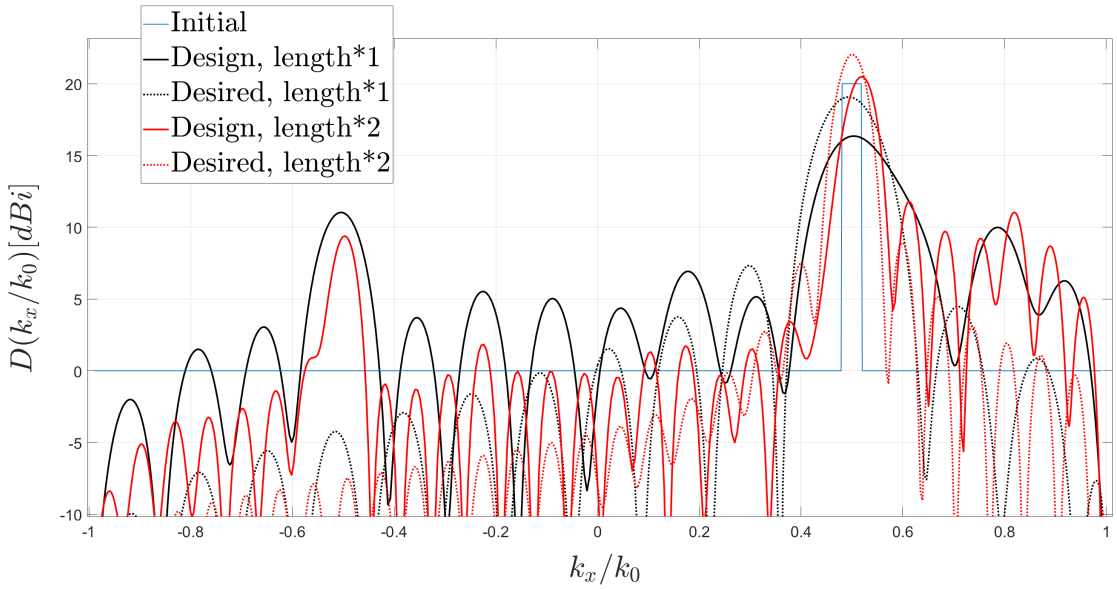

Figure 3.6: Influence of the length of the antenna on the spectral directivity in the case of the pencil beam pattern.

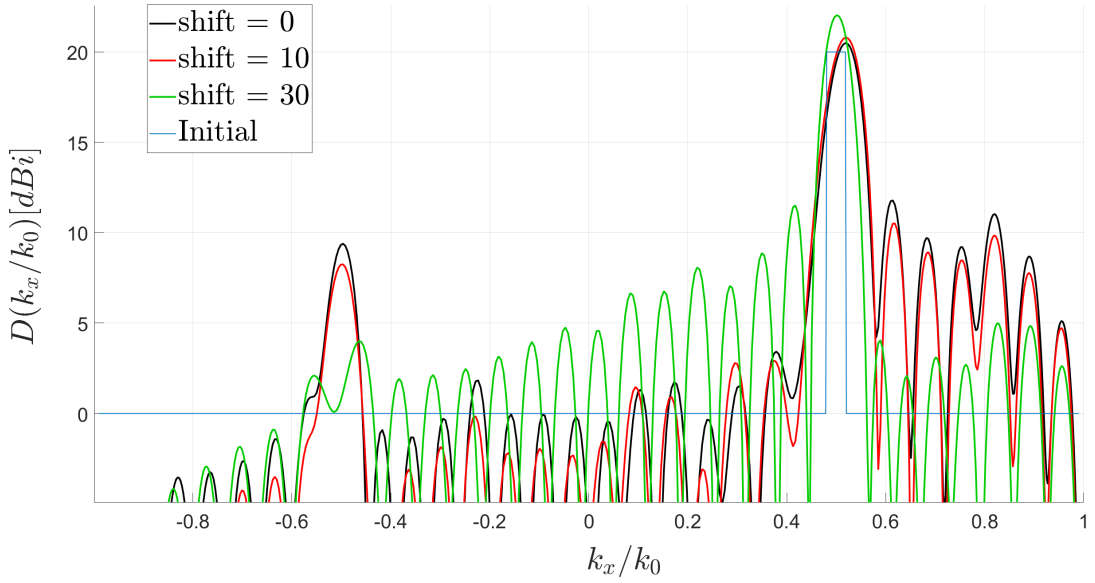

Figure 3.7: Influence of the phase shift applied to the desired pattern on the designed directivity of the antenna. The case of the pencil beam pattern is considered as well as a double antenna length.

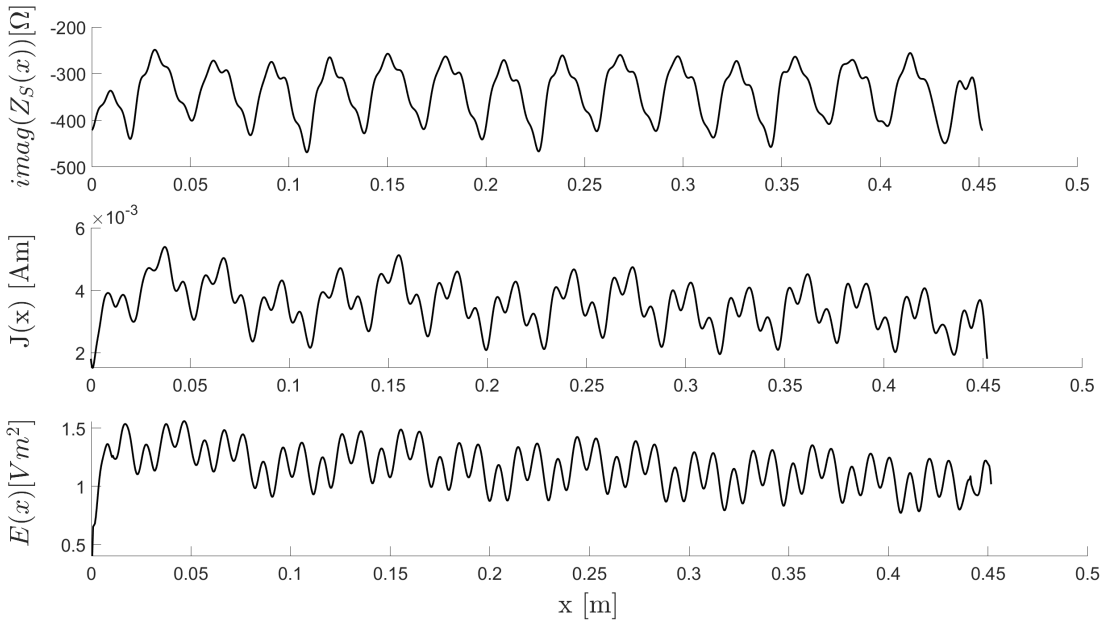

Figure 3.8: From top to bottom: the imaginary part of the surface impedance, the current distribution and the electric field along the antenna for the pencil beam pattern.

be made regarding the evolution of the electric field. The amplitude of the latter does not change much but tends to decrease along the antenna gradually. These results make sense from a physical perspective, which demonstrates good modelling of the MTS antenna.

3.3.3 Multibeams

To increase the design complexity we consider here the case of patterns with two or three pencil beams.

By keeping the parametrization determined in the previous section, results of simulations are given in Fig. 3.9 and 3.10. The main beams are well designed, but we notice a slight decrease in directivity. In addition, the level of the sidelobes is, on average, higher than expected.

The associated surface impedances, current distributions and electric fields are given in Appendix C.2 to keep enough clarity in the explanations.

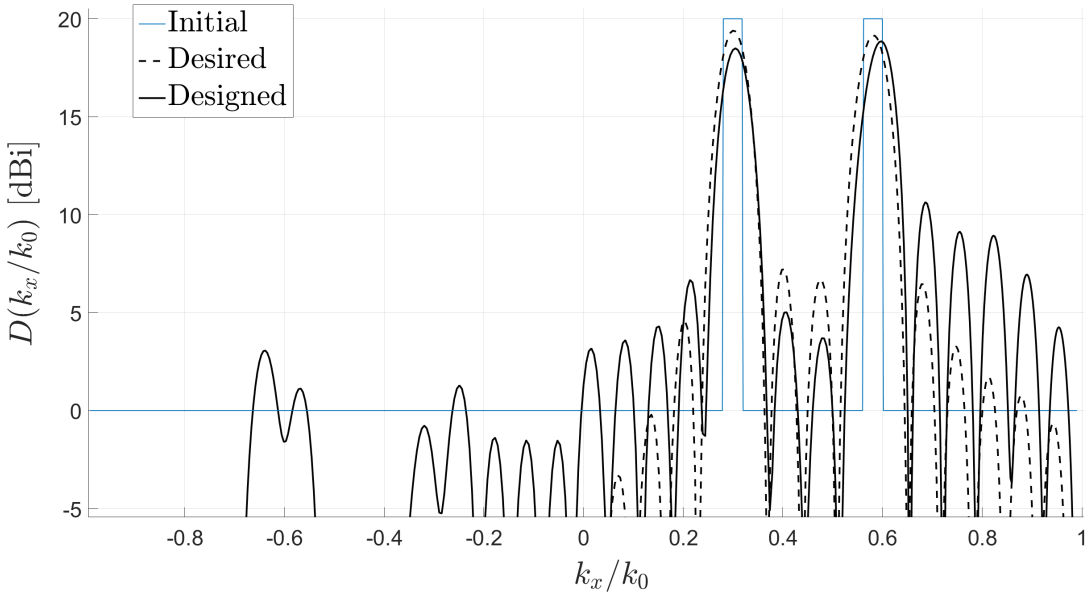

Figure 3.9: Initial and desired directivities for the pattern with two pencil beams as well as the directivity obtained after the synthesis of the surface impedance.

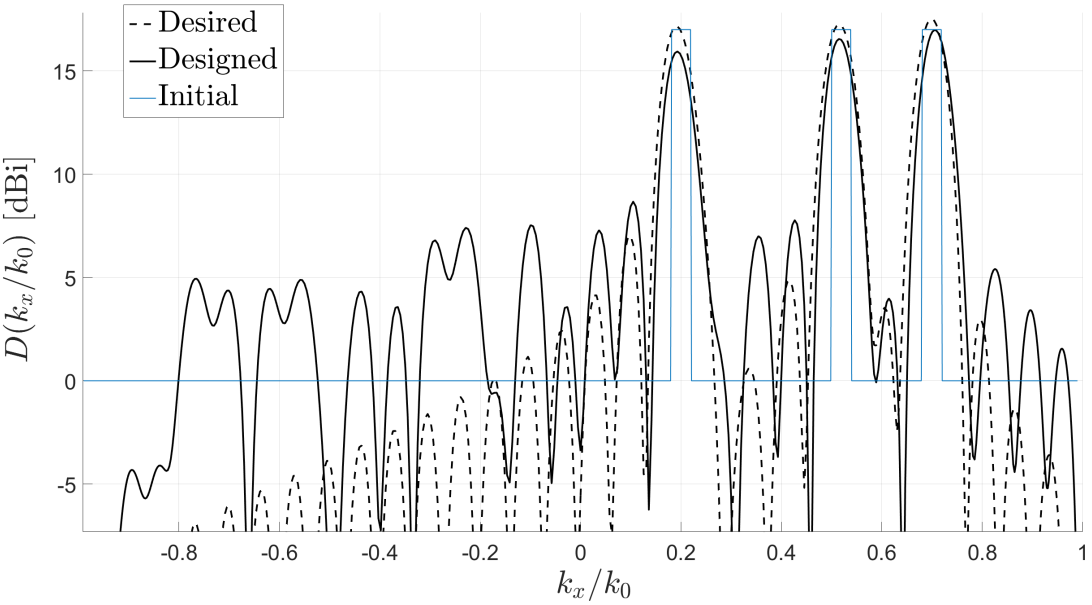

Figure 3.10: Initial and desired directivities for the pattern with three pencil beams as well as the directivity obtained after the synthesis of the surface impedance.

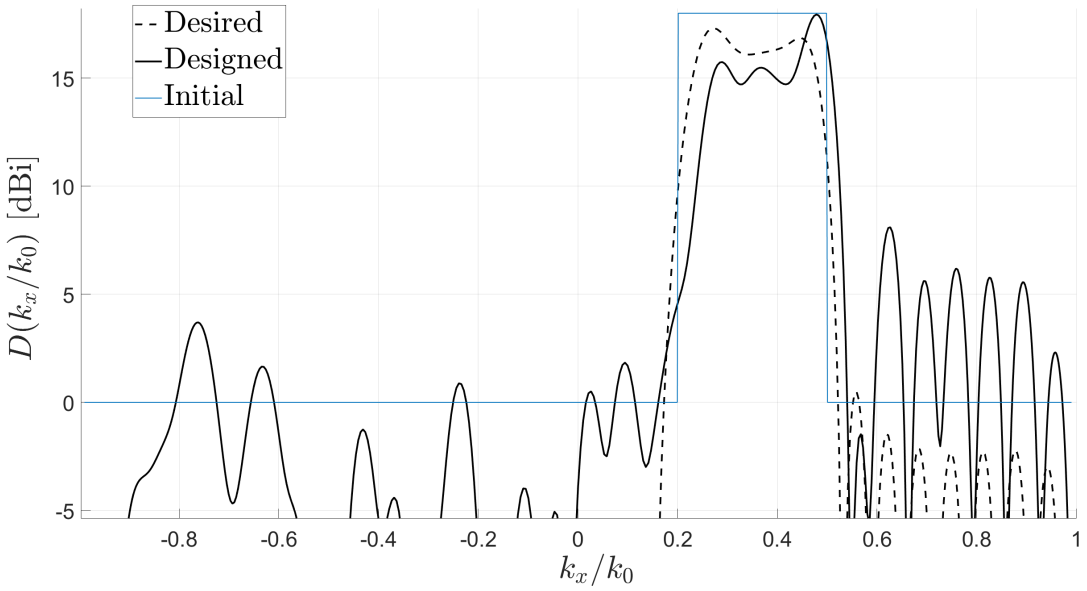

Figure 3.11: Initial and desired directivities of the flat top beam as well as the directivity obtained after designing the corresponding surface impedance.

3.3.4 Flat top beam

The goal now is to verify the ability of the design procedure to solve the inverse problem for an even more complex pattern. We consider here a flat top beam, and the parameterization used until now is still optimal. The results obtained are provided in Fig. 3.11.

A notable difference from the case of the pencil beam treated in Section 3.3.2 is the significant influence of the linear phase shift applied to the initial pattern on the performance of the design. We observe on Fig. 3.12 the impact of the shift factor s (3.24). Patterns obtained for a shift factor smaller than 30 are not correct at all.

To understand why, we look at the inverse Fourier transform of the radiation pattern $\mathbf{F_{init}}(k_x)$ to obtain the fields along the antenna (see Fig. 3.13). Based on the intuitive explanation advanced in Section 3.3.1, we can analyze the shape of the fields for the extreme cases (shift factor equal to 0 and 30) and the feasibility of their realization in practice.

- shift factor $s = 0$ The evolution of the fields results in the radiation of practically all the power at the feed level. Unfortunately, this behaviour is very complicated to achieve in practice.

- shift factor $s = 30$ The evolution of the field in this configuration is more

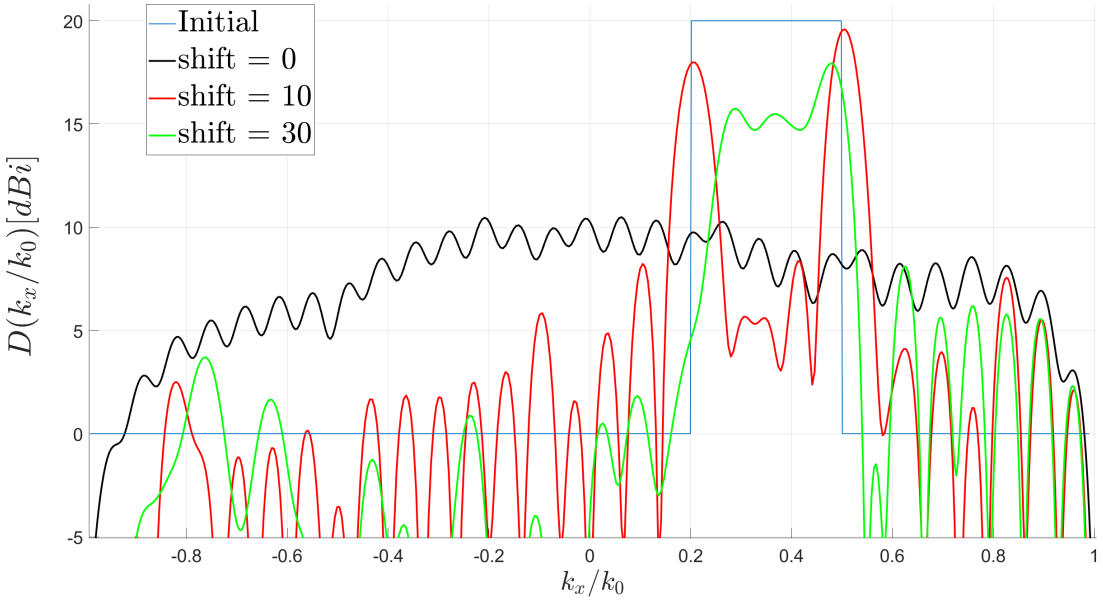

Figure 3.12: Influence of the phase shift on the designed directivity of the antenna. The case of the flat top beam pattern is considered as well as a double antenna length.

feasible in practice. The radiated power increases to be mainly released in the middle of the antenna.

From these intuitive interpretations as well as the patterns presented in Fig. 3.12, we favor the application of a linear phase factor equal to $e^{-ik_x 30}$. The corresponding pattern is given in Fig. 3.11. The main beam stands out from the sidelobes, and the antenna radiates in the expected directions despite a slight shift and loss of directivity.

3.3.5 General observations

Following the simulations, we can note a few general observations.

- The synthesis step is much faster using the entire-domain basis functions compared to rooftops. The results obtained in the two databases are identical.
- The synthesis step makes it possible to obtain patterns compliant with those desired by determining the corresponding surface impedance.
- Patterns resulting from the design exhibit an increase in the level of the sidelobes and a slight decrease in directivity compared to the expected results.

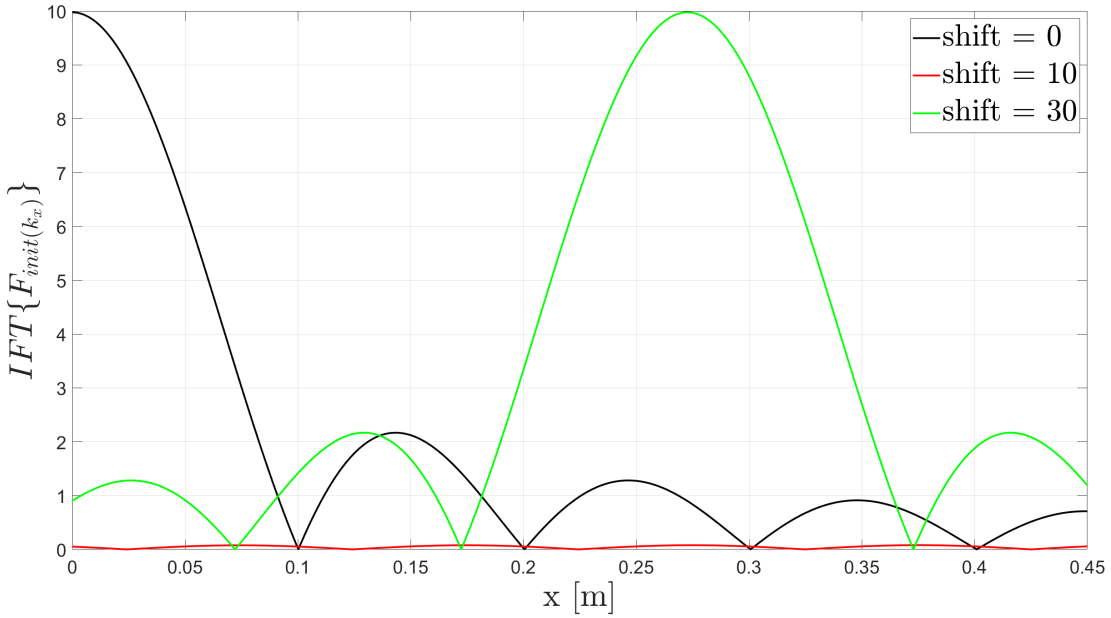

Figure 3.13: Influence of the phase shift on the inverse Fourier transform of the radiation pattern $\mathbf{F_{init}}(k_x)$ in the case of the flat top beam pattern.

- Doubling the length of the original antenna naturally allow a wider spectrum in the pattern, and hence a higher directivity.
- The influence of the phase shift parameter on the design depends on the desired pattern and must be adapted accordingly.

Chapter 4

Implementation of 1D modulated metasurface antennas

This chapter explores the last step of the design process. This step consists of implementing the surface impedance $Z_S(x)$ determined in the Chapter 3 using metallic patches. It leads to the physical structure of the antenna.

The general approach is summarized in Fig. 4.1. First, the surface of the antenna (a) is discretized into sub-wavelength unit square cells (b). In our case, these are cells of size $\lambda/7$, with λ being the free-space wavelength. Then, in the centre of each cell a metallic patch is printed (c). Its size depends on the value of the surface impedance $Z_S(x)$ evaluated at the centre of the patch. The resulting physical structure is given by the configuration (d). Those patches are finally meshed with rooftops and simulated using the MoM code of the lab to obtain the radiated pattern, noted $\mathbf{F_{impl}}(k_x)$.

To obtain the implemented IBC it is necessary to generate a database containing a series of sheet impedance values and the corresponding patch sizes. The procedure to achieve this is detailed in the next section. The chapter will end with an implementation of the surface impedances obtained in the previous chapter for the following cases: a pencil beam, multibeams and a flat top beam. We will compare the patterns $\mathbf{F_{design}}(k_x)$ directly obtained from the least-squares solution $Z_S(x)$ and already presented in Section 3.3 to the one obtained from simulation of metallic patches $\mathbf{F_{impl}}(k_x)$.

4.1 Construction of the database

The database used in this thesis has been provided based on substrate parameters and the operating frequency of the antenna (see Table 2.1). The procedure to obtain the data has therefore not been implemented or studied within the framework of the

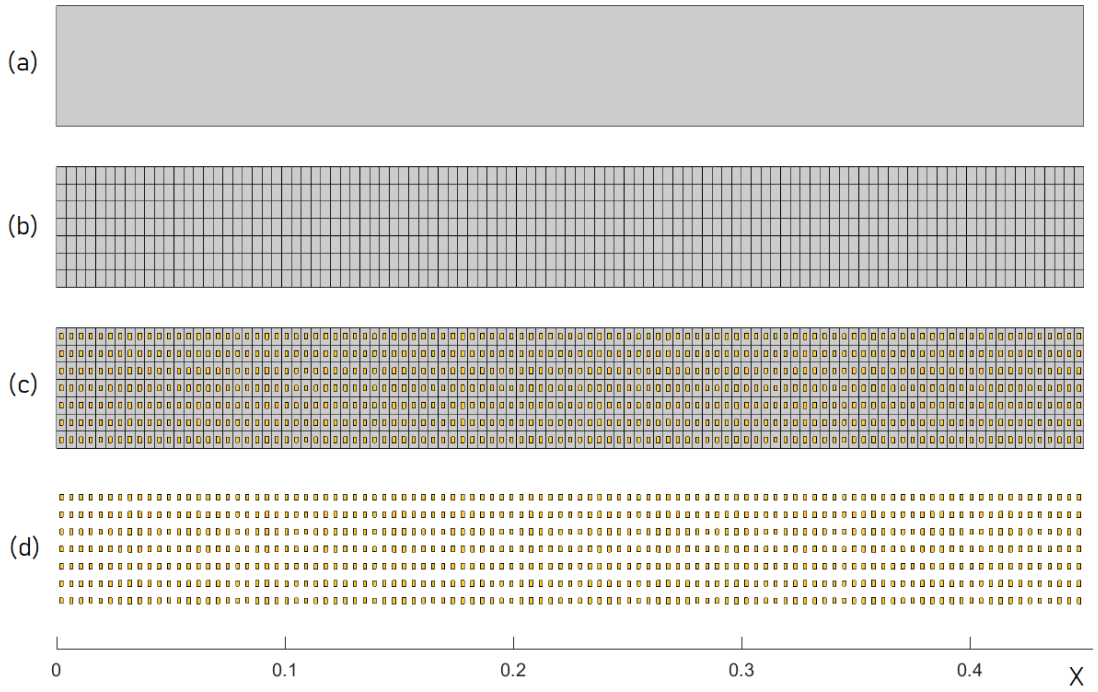

Figure 4.1: Different configurations of the surface of the MTS antenna for the implementation procedure. (a) Definition domain of the antenna on which the surface impedance $Z_S(x)$ is defined (b) Discretization of the surface with square unit cells of size $\lambda/7$ (c) Matching of the surface impedance with the metal patches (d) Final structure consisting of metal patches.

thesis. However, it is essential to give the main concepts underlying the required simulations to obtain the sheet impedance corresponding to a unique patch.

In this section, we will briefly detail the necessary steps to obtain the sheet impedance corresponding to a sub-wavelength printed patch of size smaller or equal to $\lambda/7$. The procedure is based on an essential assumption of local periodicity. This assumption means that the patch from which we want to extract the sheet impedance is immersed in a periodic environment dictated by the size of the unit cell, $\lambda/7$ in our case. In other words, the patch sees its environment as if it were periodic, which assumes a relatively smooth surface impedance. With this hypothesis, it is possible to simulate, on the substrate, an infinitely periodic lattice of these patches using a MoM code. The MoM system of linear equations is written as follows

$$\mathbf{Z_{mom}}\mathbf{i} = \mathbf{v} \tag{4.1}$$

The $\mathbf{Z_{mom}}$ matrix impedance, which equivalently describes the behaviour of a periodic lattice of patches, is only valid for a specific excitation.

$$\mathbf{Z_{mom}}\left(\mathbf{k}\right)\mathbf{i} = \mathbf{v} \tag{4.2}$$

With $\mathbf{k}$ the wave vector (k_x, k_y, k_z). In this thesis, the surface impedance is scalar which implies that it depends only on the direction $k_\rho = \sqrt{k_x^2 + k_y^2}$, the surface being isotropic.

$$\mathbf{Z_{mom}}\left(k_\rho\right)\mathbf{i} = \mathbf{v} \tag{4.3}$$

In addition, we consider here the case of a MTS antenna excited by a surface wave. In this specific case, finding a valid solution to the system (4.3) is possible regardless of whether excitation $\mathbf{v}$ exists. It is possible to find a solution of the system which satisfies Maxwell's equations and the boundary conditions without having first excited the structure. This solution is nothing else than the SW wave vector k_{sw}. Determining k_{sw} amounts to solving the following equality:

$$\det\left(\mathbf{Z_{mom}}\left(k_\rho\right)\right) = 0 \tag{4.4}$$

Now that the SW wavenumber is known, we can calculate the corresponding opaque impedance as follows

$$k_{sw} = k_0\sqrt{1 + \left(\frac{X_{op}}{\eta_0}\right)^2} \tag{4.5}$$

with X_{op} the imaginary part of the opaque impedance, and k_0, η_0 the wavenumber and the impedance of the free space respectively. One can extract the sheet impedance from the opaque impedance (4.5) by applying the procedure described in Appendix A. One finally obtains the sheet impedance corresponding to the size of the simulated patch.

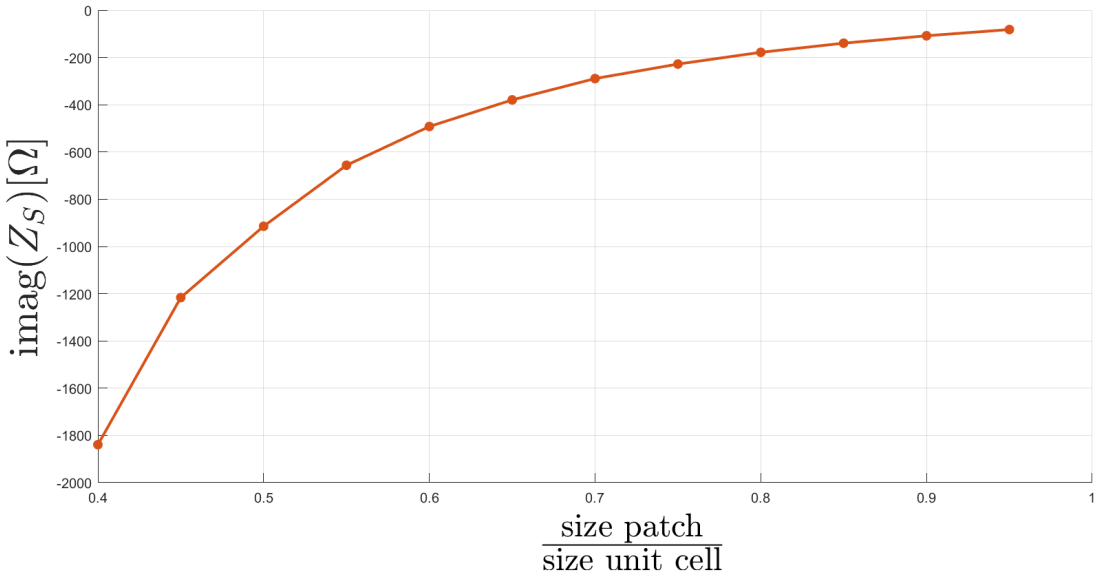

Figure 4.2: Imaginary part of the sheet impedance versus normalized patch size.

By repeating the whole procedure for different patch sizes, we can create a database, represented graphically in Fig. 4.2. In this case, 12 patch sizes have been analyzed. The interpolation of these values is necessary to have access to the sizes corresponding to any impedance values ranging from -1800 to -70 Ω. Now, suppose that the implementation of a particular surface impedance requires values outside of this range. In that case, errors are introduced, and the accuracy of the implemented IBC decreases. Fortunately, for each implementation realized in the next section, all the required sheet impedances are available from interpolation of the values contained in the database.

4.2 MoM simulations of the implemented designs

Now that the database is built, we can implement the surface impedances obtained from least-squares resolution in Chapter 3 for different radiation patterns. Then, the structures are simulated with the MoM code of the lab using the same excitation as the one used to obtain the surface impedance (2.6).

The results are given in Figs. 4.3 to 4.6. On these graphs we can see

- $\mathbf{F_{init}}(k_x)$ the pattern initially desired that corresponds to the input of the algorithm (3.8).

- the directivity computed from $\mathbf{F_{design}}(k_x)$, the pattern directly obtained from the least-squares solution $Z_S(x)$ and already presented in the Section 3.3.
- the directivity computed from $\mathbf{F_{impl}}(k_x)$, the pattern resulting from the MoM simulation of the physical structure composed of patches.

We can note some general observations common to all patterns. First of all, we notice that the general shape of the patterns before and after implementation is very similar. Following the implementation, the expected main beams are visible. However, matching the surface impedance on the metal patches introduces approximations. They mainly affect the secondary lobes, whose level, on average, has increased. We note the presence of quite high secondary lobes in the case of the pattern presenting three beams. The increase in the level of sidelobes results in a decrease in the maximum expected directivity. For pencil beams, we perceive a loss of 2 dBi and slightly more for the broader pattern where a loss of 3 dBi is observed. The pointing angles are also slightly shifted to the left following the implementation of the patches. We note an offset ranging from 1.15° to 2.12° in the case of pencil beams.

In the specific case of the pencil beam in Fig. 4.3, we also observe the presence of the backlobe in θ equal 30° after simulation of the structure made up of patches. This phenomenon is also visible in Fig. 4.4 for the case of the pattern composed of two beams. Indeed, important backlobes are located in k_x/k_0 equal to -0.6 and -0.3, which are angles of radiation in the opposite direction to the desired one. This observation certainly describes the reflection effect that can occur at the end of the antenna when all the power has not been radiated.

All inaccuracies can come from errors accumulated following the use of interpolated values from the database to define the size of the patches. Also, the relationship between the size of the patch and the sheet impedance is not perfect because it is based on the assumption of local periodicity.

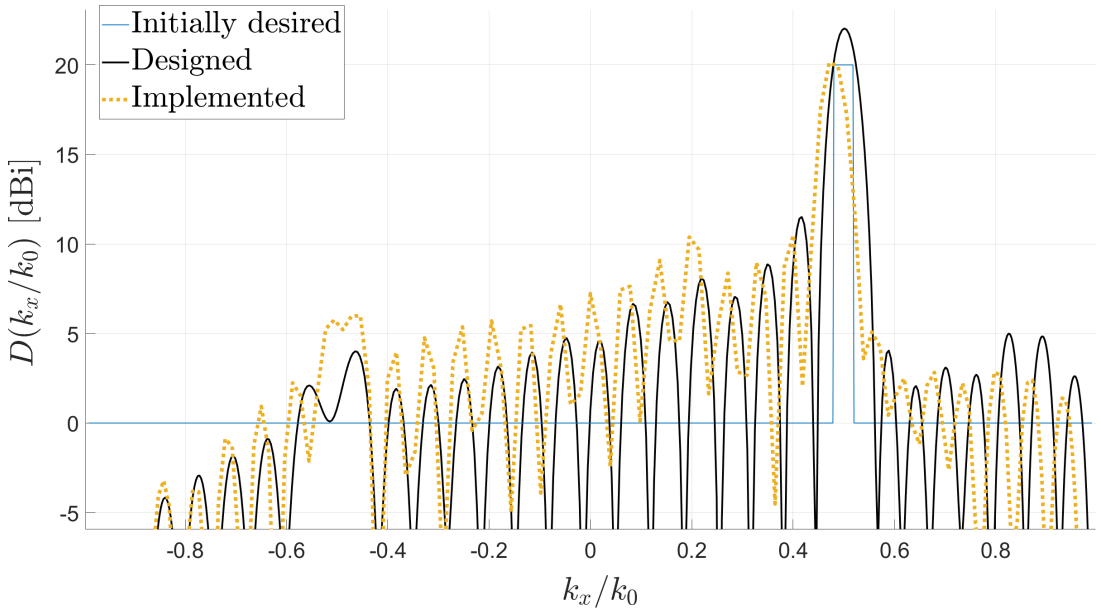

Figure 4.3: Initial desired pattern as well as the directivity resulting from the design and the one following MoM simulation of the implemented IBC with patches in the case of a pencil beam.

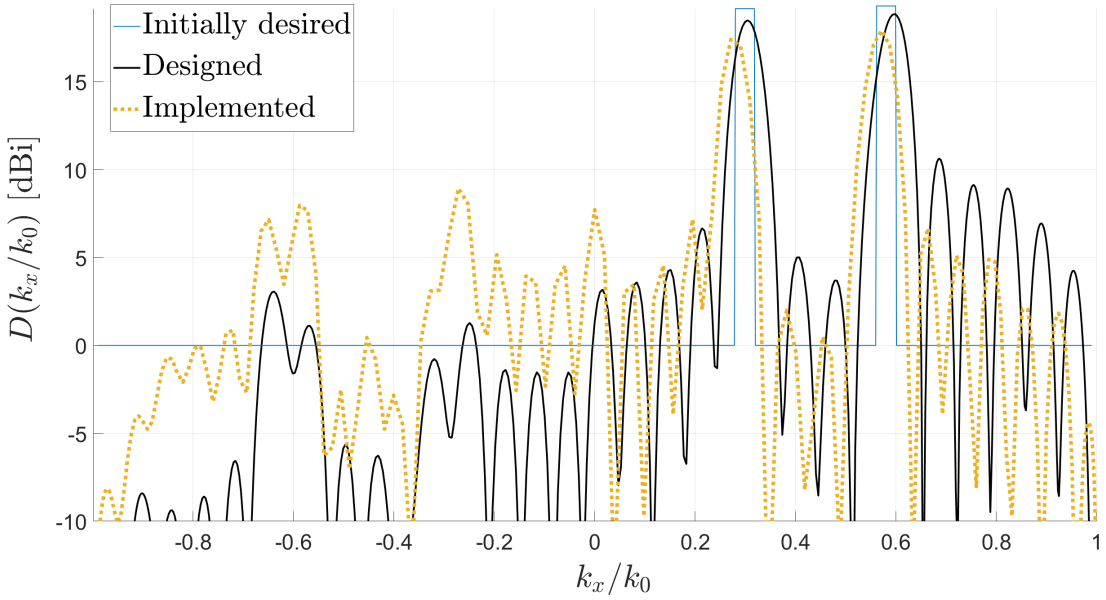

Figure 4.4: Initial desired pattern as well as the directivity resulting from the design and the one following MoM simulation of the implemented IBC with patches in the case of two pencil beams.

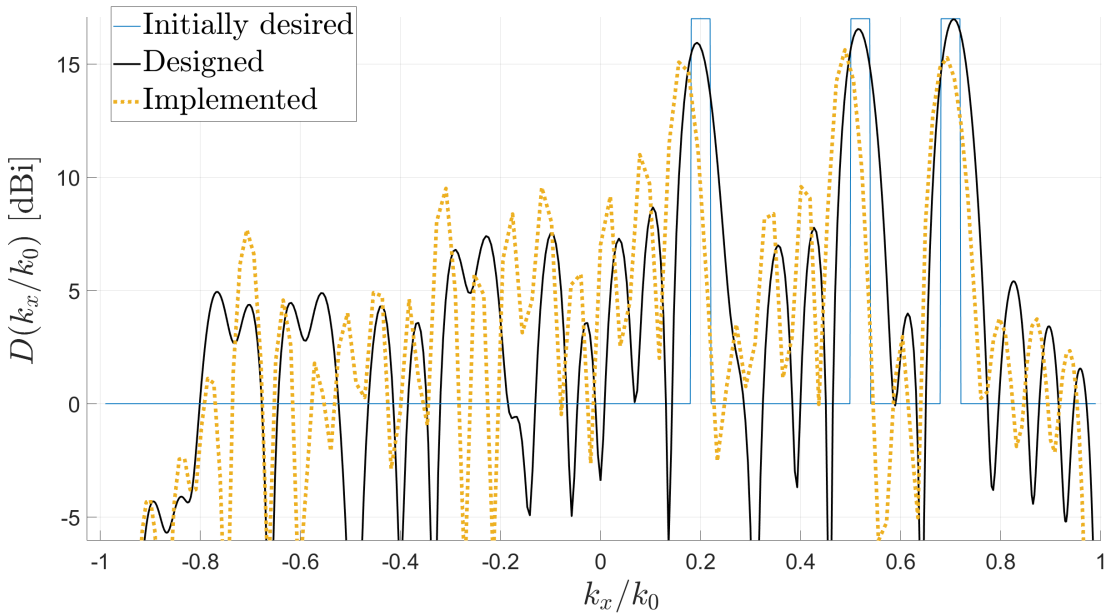

Figure 4.5: Initial desired pattern as well as the directivity resulting from the design and the one following MoM simulation of the implemented IBC with patches in the case of three pencil beams.

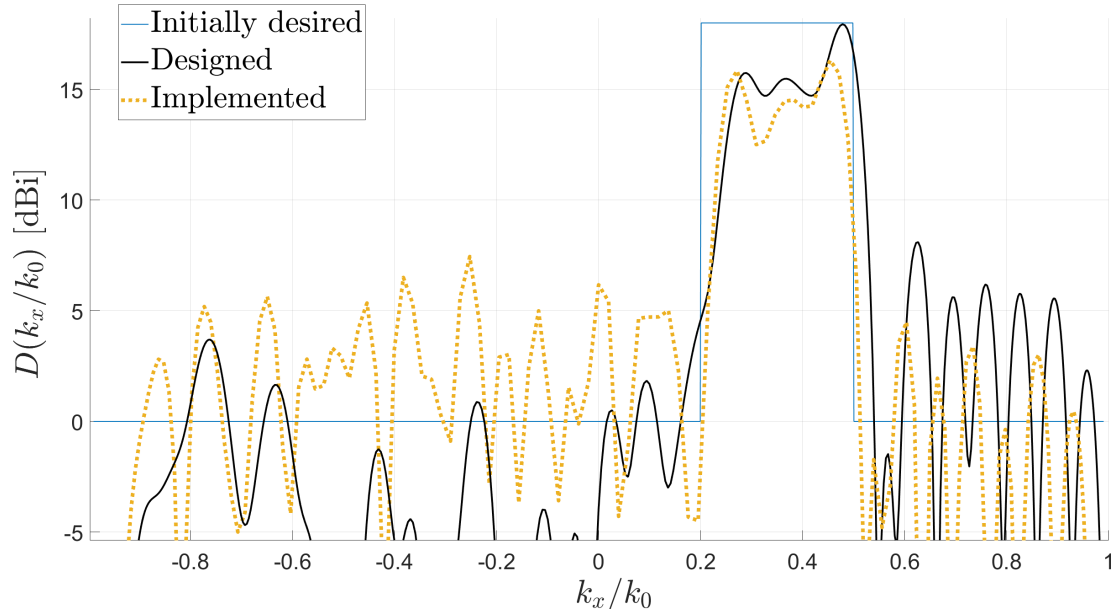

Figure 4.6: Initial desired pattern as well as the directivity resulting from the design and the one following MoM simulation of the implemented IBC with patches in the case of a flat top beam.

Conclusion and Future Works

Conclusion

This thesis developed the implementation of an analysis and design procedure for 1D modulated impedance metasurface antennas. The metasurface antenna simulation should take into account all the metal patches printed on its surface. The number of these patches is significant due to their small size, and the simulation of the whole structure requires sophisticated algorithms.

The design procedure developed in this work is based on the representation of the metasurface structure by an impedance boundary condition (IBC). The interaction of this IBC with an excitation known a priori is analyzed through the MoM formulation of an integral equation linking the fields to the currents.

The impedance profile, expanded into in a basis of appropriate functions, allows the formulation of the inverse problem. The solution of a linear system of equations allows the synthesis of IBC from desired radiation pattern, defined in amplitude and phase. This algorithm is quasi-direct because only some parameters need to be tuned to improve the accuracy of the solution. Numerical simulations were carried out using the Matlab language. They allowed the synthesis of surface impedances corresponding to patterns characterized by the presence of a pencil beam, multibeams or a flat top beam.

In the last chapter of the thesis, the resulting IBC was implemented using metal patches. The MoM simulation of the obtained structure enables the validation of the design procedure. The results demonstrate the ability of the algorithm to efficiently and quickly come up with a design that meets many of the desired radiation characteristics. Although the results are promising, attention still needs to be paid to the increase in sidelobes observed on the designed patterns. In fact, their level is much higher than expected, which leads to a slight decrease in directivity. Also, the pointing angles of all produced patterns are subject to small offsets.

Future Works

In this thesis, the excitation is modelled as a plane wave. One could pay more attention to the modelling of the feed. Indeed, it would be interesting to model it more precisely to obtain a better representation of the antenna excitation and evaluate the compling between the feeding currents and the surface wave.

The characterization of an MTS antenna operating in the X band was one of the initial objectives of the thesis, which could not be achieved. However, this goal is still relevant today, with a specific focus on the control of the radiated near field. The work accomplished would allow the optimization and synthesis of an antenna design to finally produce a prototype. Primary tests in an anechoic chamber would allow the comparison of the antenna's performance with the simulations. Then, other specific near-field measurements could be carried out at UCLouvain using a test bench equipped with Hall probe magnetic sensors.

The observation of the near field makes sense in the study of metasurface antenna because this technology allows the control of waves at a sub-wavelength scale. This capability makes these antennas good candidates for the development of technologies such as modern imaging, sensing, or communications systems [8]. Establishing precise near-field shaping is one of the challenges that MTS antennas still need to address.

Another challenge related to the ability to control the orientation of beams is beam scanning. Beam scanning is an essential feature of developed communication systems as 5G to track users. We have seen in the thesis that obtaining radiation characteristics is possible based on a particular excitation and configuration of printed patches. However, once determined, the physical structure of the antenna is fixed and difficult to adapt to modify the pointing angle of the pattern. We find in the literature solutions offering prototypes of antennas with electronically or mechanically tunable textured surfaces. Those techniques allow beam scanning but induce a much more complicated structure [10]. More recently, numerical simulations demonstrated the possibility of beam scanning by acting on the feeding and not the structure of the antenna. This technique is based on multi-fed phased MTSs and thus opens a new way to meet beam scanning property [8].

Bibliography

1. Faenzi, M. & Minatti, G. Metasurface Antennas New Models Applications and Realizations. *Scientific Reports* **9** (2019).
2. Hu, J. & et al. A Review on Metasurface: From Principle to Smart Metadevices.
3. L. Holloway, C. An Overview of the Theory and Applications of Metasurfaces The Two-Dimensional Equivalents of Metamaterials (2012).
4. Quevedo-Teruel, O. & et al. Roadmap on metasurfaces. *Journal of Optics* **21** (2019).
5. *Example of metamaterial* `https://www.smart2zero.com/news/metamaterials-poised-disrupt-5g-autonomy-and-connected-vehicles` (2021).
6. Minatti, G. & et al. Modulated Metasurface Antennas for Space: Synthesis, Analysis and Realizations. *IEEE Transactions on antennas and propagation* **63** (2015).
7. Guissard, A. & Craeye, C. *Notes de cours chapitre 4, LELEC2910: Antennes et propagation*
8. Bodehou, M. *Modulated Metasurface Antennas, Analysis and Direct Numerical Synthesis* PhD thesis (2020).
9. Sievenpiper, D., Schaffner, J., Lee, J. & Livingston, S. A Steerable Leaky-Wave Antenna Using a Tunable Impedance Ground Plane. *IEEE Antennas and Wireless Propagation Letters* (2002).
10. F. Sievenpiper, D. Forward and Backward Leaky Wave Radiation With Large Effective Aperture From an Electronically Tunable Textured Surface. *IEEE Transactions on antennas and propagation* **53** (2005).
11. Sipus, Z., Barbaric, D. & Bosiljevac, M. Analysis of Curved Metasurfaces with Spatially-Varying Impedance Distribution (2019).
12. Kayani, H. A. PhD thesis AppendixA : Green's Functions in Layered Substrates.
13. *Antenna directivity and gain* `https://m.eet.com/images/common/rfdesignline/2010/06/C0581Ch3pt2.pdf`.

14. Sarkar, T., Djordjevic, A. & Kolundzija, B. Method of Moments Applied to Antennas.

15. Introduction to Finite Element Methods for Electromagnetic fields and coupled problems. http://dreaden.ulyssis.org/em.pdf.

16. Harrington, R. Origin and Development of the Method of Moments for Field Computation. *IEEE Antennas and Propagation Society Magazine.* (2021) (June 1990).

17. *The Math Works, Inc. MATLAB. Version 20218a Student Use, The Math Works, Inc., 2020. Computer Software.* www.mathworks.com/.

18. Patel, A. & Grbic, A. A printed Leaky-Wave Antenna Based on a Sinusoidally-Modulated Reactance Surface (2011).

19. Bodehou, M., Craeye, C., Huynen, I. & Martini, E. A Quasi-Direct Method for the Surface Impedance Design of Modulated Metasurface Antennas (2018).

20. *Representation of a leaky-wave structure* https://asa.scitation.org/doi/full/10.1121/1.4949544.

Appendices

Appendix A

Definition of basis functions for MoM simulations

In the MoM code of the EPL antenna laboratory, the rooftop basis functions are defined as shown in Fig. A.1. The mesh represented here contains basis functions which overlap in the $\hat{y}$ direction. As for all the MoM simulations generated in this thesis, the rooftops have their z component equal to zero because they are defined in a single plane, that of the antenna.

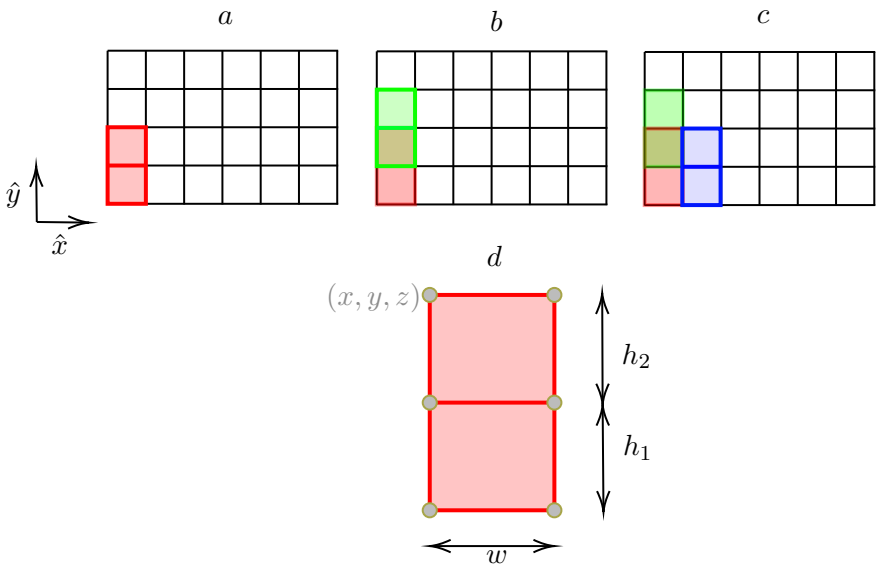

Figure A.1: Definition of rooftop basis function used in the MATLAB code for MoM simulation. (a) Mesh with a single basis function, (b) Mesh with two basis functions along $\hat{y}$, (c) Mesh with three basis functions along $\hat{y}$, (d) Basis function parameters: width w, upper length h_2, lower length h_1 and coordinates (x, y, z) of the six position points in gray.

Appendix B

Extraction of sheet impedance from opaque impedance

This appendix details the extraction of the sheet impedance Z_s from an opaque impedance Z_{op} defined as follows (for 1D case)

$$Z_{op} = jX_0 + P(x) \tag{B.1}$$

with X_0 the average opaque impedance and $P(x)$ the modulation.
The mathematical developments are based on the theory of transmission lines. As we know the mode (propagation of TM SW) which propagates in the structure we can design the equivalent transmission line (see Fig. B.1).

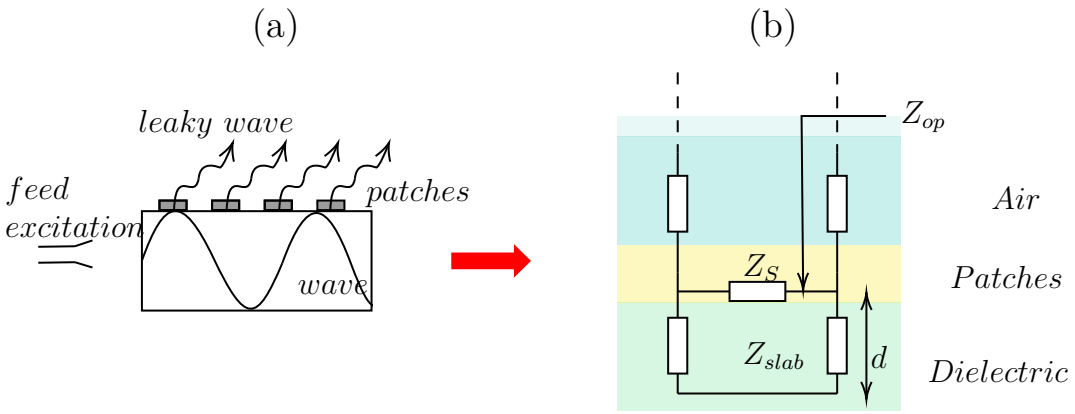

Figure B.1: Antenna structure and the equivalent transmission line.

Let us define the following notations:

- k_{sw} and k_1 the wavenumber of the surface wave and the wavenumber in the substrate

- k_{z1} the z-component of the wavenumber in the substrate
- η_0 and η_1 the free-space impedance and the impedance of the substrate
- d_{slab} the thickness of the substrate

We now can compute the opaque admittance and the admittance of the dielectric layer and the substrate

$$Y_{op} = \frac{1}{Z_{op}} \tag{B.2}$$

$$Y_{diel}^{TM} = \frac{k_1}{\eta_1 k_{z1}} \tag{B.3}$$

$$Y_{slab}^{TM} = -iY_{diel}^{TM} \frac{\cos\left(k_{z1} d_{slab}\right)}{\sin\left(k_{z1} d_{slab}\right)} \tag{B.4}$$

As the sheet impedance appears in parallel with the dielectric impedance, we can substract the admittance contribution of the substrate from the opaque admittance to obtain the sheet contribution.

$$Y_s = Y_{op} - Y_{slab}^{TM} \tag{B.5}$$

Finally the sheet impedance Z_s is calculated very simply by inverting the previous equality

$$Z_s = \frac{1}{Y_s} \tag{B.6}$$

Appendix C

Additional information on 1D MTS antenna synthesis

C.1 Pencil beam pattern

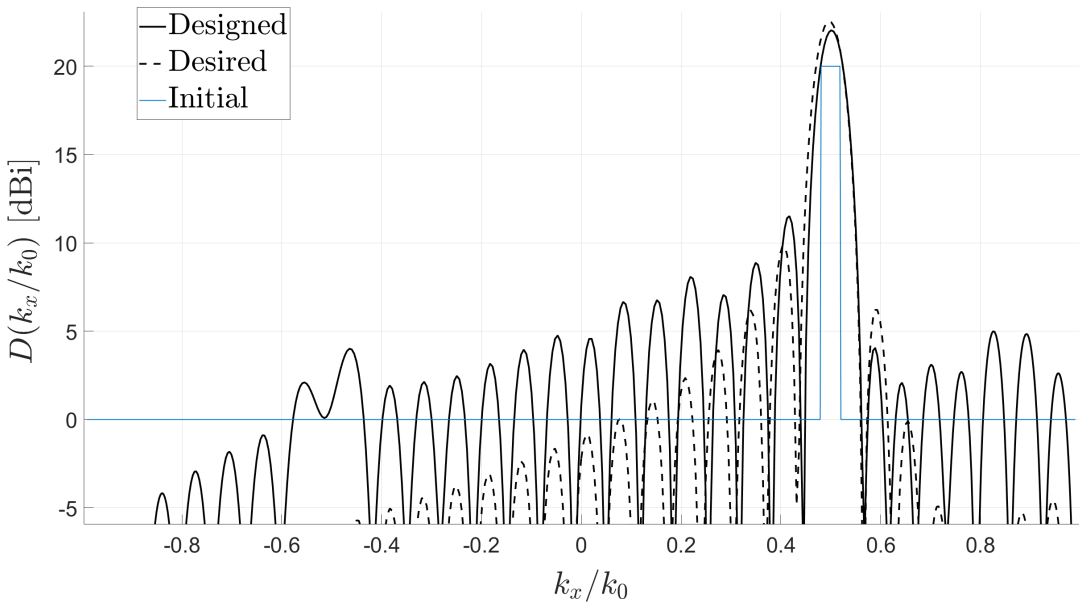

Figure C.1: Initial and desired directivities of the pencil beam pattern as well as the directivity obtained after designing the corresponding surface impedance.

C.2 Multibeams pattern

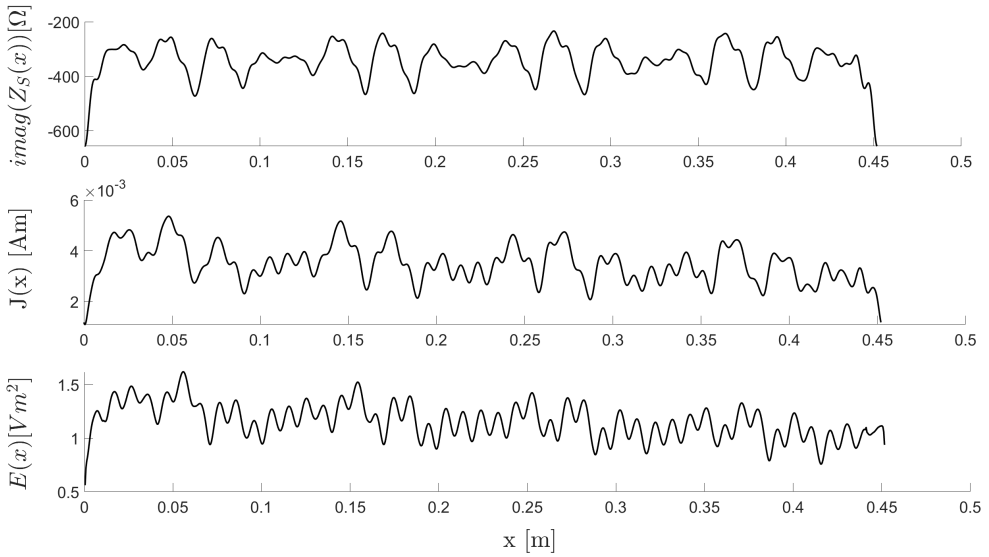

Figure C.2: Imaginary part of the surface impedance, the current distribution and the electric field along the antenna for the case of a double pencil beam pattern.

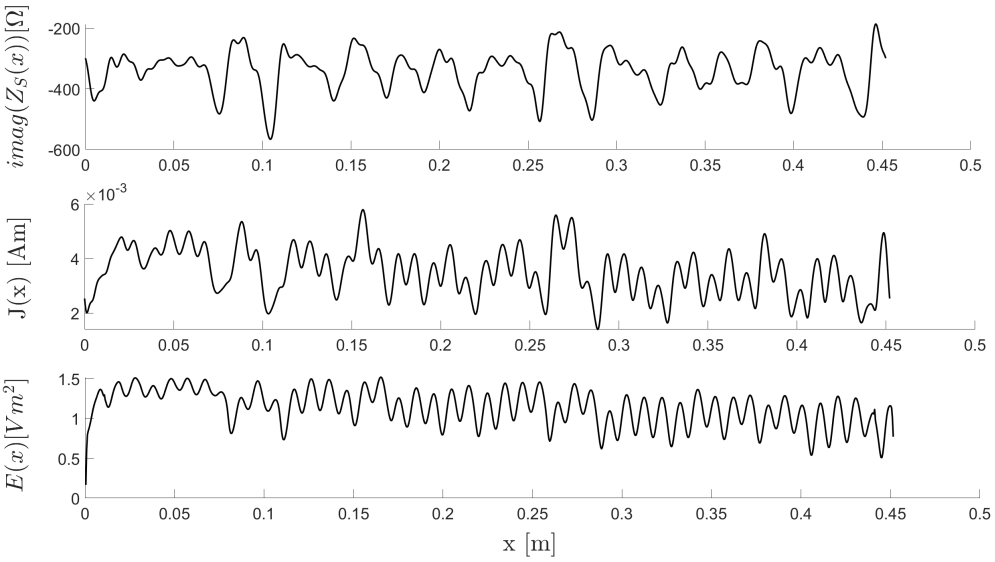

Figure C.3: Imaginary part of the surface impedance, the current distribution and the electric field along the antenna for the case of a three pencil beam pattern.

C.3 Flat top beam

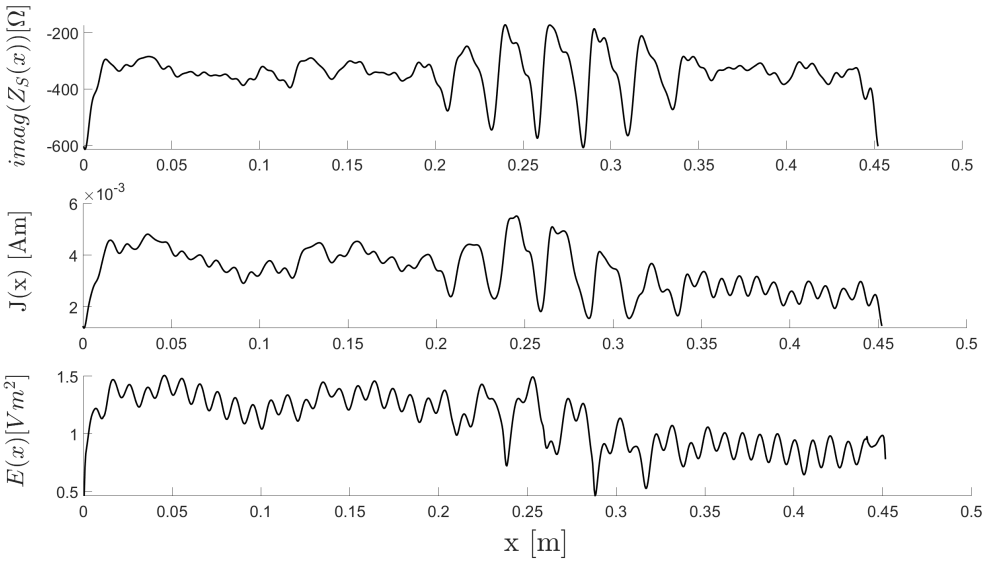

Figure C.4: Imaginary part of the surface impedance, the current distribution and the electric field along the antenna for the case of a flat top beam pattern.

UNIVERSITÉ CATHOLIQUE DE LOUVAIN
École polytechnique de Louvain
Rue Archimède, 1 bte L6.11.01, 1348 Louvain-la-Neuve, Belgique | **www.uclouvain.be/epl**